Supplementary Materials for

Spring-loaded unraveling of a single SNARE complex by NSF in one round of ATP turnover

Je-Kyung Ryu, Duyoung Min, Sang-Hyun Rah, Soo Jin Kim, Yongsoo Park, Haesoo Kim, Changbong Hyeon, Ho Min Kim, Reinhard Jahn,* Tae-Young Yoon*

*Corresponding author. E-mail: rjahn@gwdg.de (R.J.); tyyoon@kaist.ac.kr (T.-Y.Y.)

Published 27 March 2015, *Science* **347**, 1485 (2015)
DOI: 10.1126/science.aaa5267

This PDF file includes:

Materials and Methods

Protein constructs.

Bovine α-SNAP and Chinese hamster NSF were cloned into pET28a with His_6 tags and thrombin cleavage sites for removing the His_6 tags. All SNARE proteins were derived from *Rattus norvegicus*. For fluorescence assays, the soluble part of VAMP2/Synaptobrevin (sVAMP2) (1-96) and full-length of VAMP2 (1-116) were cloned into pGEX-KG vectors containing GST-tags as described (*4*), followed by cysteine-mutation at positions R30 or A82 for labeling Cy3 at the N- or C-terminal of sVAMP2, and A82 for full-length VAMP2. For acceptor complex assembly, a truncated version of syntaxin-1A without the N-terminal Habc domain (183-288) and C-terminal VAMP2 (49-96) were cloned together into a pETDuet-1 vector without any affinity tags as previously described (*32, 33*). In addition, cysteine-free variant of SNAP-25A was cloned into pET28a (*34*). The acceptor complex was assembled by co-expression of the two plasmids (*20*) (fig. S1B). For FRET experiments, cysteine residues in the pETDuet-1 vector were substituted to serine. This was followed by substituting residues K79 or E27 in SNAP-25A to cysteine for Cy5 labeling at the C- and N-terminals, respectively (Fig 2A and fig. S3A). Those residues were chosen as they are facing the outer side of the SNARE complex and are in close proximity with the respective labeling positions at sVAMP2. The SNARE proteins used in magnetic tweezers are as follows: syntaxin-1A (amino acids 191–267, SNARE motif with C-terminal linker), SNAP-25 (amino acids 1–206 with four native cysteines replaced by alanines) and VAMP2 (amino acids 1–97 lacking the trans-membrane domain). For DNA-handle attachment, certain residues outside linker domains were replaced with cysteines (amino acid 266 for syntaxin-1A and amino acid 97 for VAMP2). Since these residues are on the exterior surface of the SNARE complex (fig. S10A), we can attach the DNA handles while minimizing perturbation to the formation of the four-helix bundle (*4, 35-37*). For the force-ramp experiment repeating unzipping and rezipping, the amino acids in the -7 layer were additionally replaced with cysteines (amino acid 202 for syntaxin-1A and amino acid 32 for VAMP2 in position a of the heptad repeat). Because these residues in 'a' position of heptad repeat are in close contact with one another (fig. S13C), a disulfide bond spontaneously forms, knotting the N-terminal end of the SNARE complex (*4, 36*).

Protein expression and purification.

All proteins were expressed in the *E. coli* strain Rosetta (DE3) pLysS (Novagen). Acceptor complexes were produced by co-expression and purified essentially as described. The final product was confirmed using 15 % SDS-PAGE (*20*) (fig S1B). All other proteins were purified via Ni-NTA or glutathione resins (*4, 10, 38*) followed by gel filtration chromatography or ion exchange chromatography (acceptor complexes) on an ÄKTA FPLC system, following previously established protocols. The structure of NSF was confirmed using negative staining TEM (*2, 11, 12, 39, 40*).

Protein labeling.

SNAREs with cysteine modifications were labeled with cyanine maleimide dyes as described (*41, 42*). All labeling efficiencies were higher than 70 % (fig. S3B). SNARE complex formation of the constituents were confirmed by comparing FRET signals from mixing SNAREs labeled both at the N-terminal and SNAREs labeled at opposite ends (*42*) (fig. S3E). Fluorescence was measured using an EnSpire plate reader (Perkin Elmer).

Vesicle reconstitution of acceptor complexes.

Purified lipids in 2:1 chloroform:methanol were purchased from Avanti Polar Lipids. A mixture composed of 44 % POPC, 25 % Cholesterol, 12 % DOPS, 15 % DOPE, 3 % PIP2, and 0.7 % Biotin-DPPE was prepared in cleaned vials. 1% lipidic dye DiI (Invitrogen) was included if the number of immobilized vesicles on the imaging surface was to be measured (fig. S1C). Solvent was removed using nitrogen gas and dried further via vacuum pumping overnight. The dried lipid film was solubilized with 3 % (w/v) n-octyl-β-D-glucopyranoside (OG) containing buffer (50 mM HEPES, 150 mM NaCl, pH 7.4) to make 15 mM lipid solution, which was incubated at 4 °C with gentle shaking for 1 hr. The lipid solution was mixed with acceptor complex and the final OG concentration was set to 2 %. For single color fluorescence assays, 1:1,000 protein to lipid ratio was used. For single-molecule FRET assays, the protein to lipid ratio was set to 1:10,000 or 1:15,000 in order to have a high proportion of vesicles containing a single SNARE complex. The protein-lipid-OG mixtures were incubated with shaking for 1 hr. This was followed by threefold dilution or addition of SM-2 bio-beads (Bio-Rad) to lower the detergent concentration below the critical micelle concentration. In the former case, bio-beads were added to remove detergents as well.

To incorporate SNARE complexes with full-length VAMP2, the complexes were first formed by mixing the acceptor complexes and full-length VAMP2 in 1 % OG micelles followed by shaking the mixtures for 1 hr. Then, we mixed SNARE complexes with lipid-OG micelles which were made by 1 hr incubation (1:20,000 protein to lipid ratio was used). The mixture was diluted 3 times with detergent-free buffer. The residual detergents were removed by SM-2 bio-beads.

Single-molecule fluorescence assay for disassembly of SNARE complex.

A piranha-cleaned quartz slide was coated with 99:1 (mol/mol) mPEG/biotin-PEG (Laysan). This PEG-treated quartz slide was placed as the bottom surface of a microfluidic chamber for prism type total internal reflection (TIR) microscopy as described (*21, 38*). 0.1 mg/ml Neutravidin (Molecular Probes, Invitrogen) or Streptavidin was incubated on the PEG slide for 5 minutes. The acceptor vesicles (10 μM [Lipids]), containing biotin-DPPE and acceptor complex, composed of syntaxin-1A and SNAP25 (*20*), were immobilized on the PEG surface by biotin-Avidin binding for 5 min. About 3,000 vesicles were immobilized per× μm^2 field of view (fig. S1C). As the average distance between immobilized vesicles (1.16 μm) is much larger than the size of the reconstituted vesicles, events from interactions of multiple vesicles could be ignored. After vesicle immobilization, 10 nM of the soluble part of VAMP2 (sVAMP2), labeled with a cyanine dye (Cy3), was injected to form SNARE complexes for 5 min at 37 °C, resulting in appearance of fluorescence spots when viewed with total internal reflection (TIR)

microscopy (Fig. 1, B and D, and fig. S1, D to G). After removing free Cy3-sVAMP2 using laminar flow, 1 μM of α-SNAP was injected and incubated for 3 min. For functional tests, free α-SNAP was washed out and 150 nM NSF and 1 mM ATP was injected with 10 mM Mg^{2+} for 5 min (Fig. 1A and fig. S1A). All NSF concentrations denote hexameric concentrations. For negative control, 1 mM EDTA was included instead of Mg^{2+}. For snap-shot analysis, the number of Cy3-sVAMP2 incorporated vesicles was counted using Molecule Identifier in the SMET package (http://tylab.kaist.ac.kr/SMET) that detects local Gaussian maxima in the TIR fluorescence images (*43*) that were recorded by an electron-multiplying charge-coupled device (iXon DU897v, Andor technology). Disassembly of SNARE complexes can be quantified by measuring how many fluorescence spots have disappeared during reaction (Fig. 1, B and D)

To check that one-round ATP binding and hydrolysis is sufficient for SNARE complex disassembly, α-SNAP-SNARE complex was made using the same procedure as for functional tests (Fig 1E and fig. S2A). 85 nM NSF, 1 mM ATP, and 1 mM EDTA (instead of Mg^{2+}) were injected to form NSF-SNAP-SNARE complex and was incubated for 3 min. After removing unbound molecules, only Mg^{2+} ions were injected and incubated for 5 min. We confirmed disassembly using both snap-shot and real time analysis. All SNARE complex disassembly experiments were done in 50 mM HEPES, 50 mM or 150 mM NaCl, pH 7.4.

To measure the disassembly of the SNARE complex with full-length VAMP2, we used the SNARE complex incorporated vesicles prepared as described above. During reconstitution, we used acceptor complexes with Cy3-labeled SNAP25 and unlabeled full-length VAMP2 (fig. S7A). Disassembly was confirmed by measuring the number of Cy3-SNAP25 incorporated vesicles imaged using snap-shot analysis.

Single-molecule immunolabeling experiment.

To detect α-SNAP and NSF in our single molecule assay, acceptor vesicles with lipid concentration of 30 μM, 300 nM unlabeled sVAMP2 (A82C), 10 μM of α-SNAP were used as in the single-molecule/single-color fluorescence assay for SNARE complex disassembly (fig. S2B). 0.1 μg/mL α-SNAP antibody (Synaptic Systems) was added. After 5 min incubation, Alexa647-labeled anti-mouse IgG (goat, Jackson ImmunoResearch) was added and incubated for 5 min. After removing all unbound molecules, the number of fluorescent spots was counted in an imaging area (Fig. 1F). For NSF detection, 1.7 μM NSF was used, and the primary antibody of NSF was added after NSF, ATP, and EDTA injection onto SNAP-SNARE complex (fig. S2C). Binding of NSF binding, which only occurred when the SNARE complexes were loaded with α-SNAP, was dependent on ATP, indicating formation of the 20S particle on our imaging plane (*15*) (Fig. 1G). We repeated the single-molecule immunolabeling experiment and found that the NSF hexamer was dissociated from the surface vesicles after disassembly whereas simple infusion of ADP did not trigger NSF release (*1, 15*) (fig. S2, D and E).

Single-molecule fluorescence real-time traces.

Movies from a fixed imaging area was taken for 180 sec using Image Recorder in the SMET package (*43*). Imaging buffer [2.5 mM PCA, 50 nM PCD, 5 mM Trolox (*44, 45*)] was added just before imaging to enhance the photostability of dyes for all fluorescence experiments unless otherwise specified. For one-round ATP hydrolysis conditions, the

filming started immediately after 10 mM Mg^{2+} injection. For excess ATP and NSF conditions, the filming started after 150 nM NSF, 1 mM ATP, and 10 mM Mg^{2+} were injected to the SNAP-SNARE complex. For both cases, the SNARE complex disassembly event was identified and tracked from the movie. For quantitative analysis of the disassembly kinetics, stepwise decrease of Cy3 signals were identified by a custom-written MATLAB (Mathworks) code that uses the Schwarz information criteria (*41, 46*) (fig. S2, F and G).

Single-molecule FRET experiment.

For single-molecule FRET assays, Cy5-labeled SNAP-25 was used to assemble the acceptor complex. To achieve a high proportion of vesicles containing only one SNARE complex, a protein to lipid ratio of 1:10,000 or 1:15,000 was used for acceptor vesicle reconstitution. For SNARE complex formation, acceptor vesicle of 100 μM lipid concentration was incubated with 20 nM Cy3-sVAMP2 in 50 mM HEPES (pH 7.4), 1 M NaCl, 1 mM TCEP for 15 min. After four-fold dilution of the mixture, SNARE complex incorporated vesicles were immobilized on the surface. The number of sVAMP2 and acceptor SNARE incorporated vesicles was confirmed by photobleaching steps of Cy3 and Cy5 using both red and green lasers (fig. S3, C and D). In the case of SNARE complexes with full-length VAMP2, we reconstituted vesicles with SNARE complexes formed by mixing acceptor complexes with Cy3-labeled SNAP25 and Cy5-VAMP2 (Fig. 2F).

Raw fluorescence signals were first filtered with a 550 nm long-pass filter. A 635 nm dichroic mirror (Chroma) separated the signals into Cy3- and Cy5- signals, which were then arranged into a dual-view alignment for two-color imaging. The two-color images were recorded simultaneously using an electron-multiplying charge-coupled device (Andor). From real-time movies, individual SNARE complexes in single vesicles were identified and their fluorescence intensities were extracted using Molecule Identifier in the SMET package (*43*), in which a Gaussian mask was applied to reduce noise. FRET values were calculated using $E = \frac{I_A}{I_D + I_A}$, where I_A and I_D are the fluorescence intensities recorded in the Cy5 and Cy3 channels, respectively.

Electron microscopy.

2 μL of purified NSF (50ug/ml) was incubated with 1 mM ATP and 1 mM EDTA to reconstitute ATP state. The mixture was applied to glow-discharged copper grids coated with carbon film, and negatively stained with 0.75% (w/v) uranyl formate. Negatively stained grids were examined under a Tecnai T120 microscope operated at 120 kV using a nominal magnification of 52,000x (2.1A/pixel, FEI Eindhoven). Images were recorded with an FEI Eagle 4 K x 4 K CCD camera, using a defocus of - 1.2 um and an electron dose of ~30 e^- per $Å^2$.

Electron microscope image processing.

Particles were semi-automatically selected using EMAN2 boxer and bad particles were manually excluded (*47*). 3,552 particles were selected from 100 micrographs and were subjected to three rounds of multivariate statistical analysis (MSA) classification and multi-reference alignment (MRA). 2D reference-free image analysis was performed using

IMAGIC (*48*). Representative two-dimensional class averages for NSF hexamers in the ATP state are shown in Fig. 1C.

DNA handle attachment to SNARE complex.

For single-molecule magnetic tweezers experiments, we attached DNA handles to a SNARE complex to prevent a magnetic bead from binding to glass surface non-specifically and to confirm a single hybrid molecule from force-extension curves of DNA handles. The handles were connected at the C-terminal end of the linker domain of the SNARE complex (fig. S10A). For DNA handle preparation, two types of 512 bp DNA (biotin- and digoxigenin-modified handles) were PCR-amplified using λ DNA template, forward primer CATGTGGGTGACGCGAAA with a 5' thiol modifier C6 S-S and reverse primer TCGCCACCATCATTTCCA with either 5' biotin or 5'digoxigenin (each 0.4 ml and 2 ml). The disulfides of thiol modifiers of the PCR products were reduced to thiol groups by 100 mM DTT for 1 h at 37 °C and then activated with 10 mM DTDP for thiol-disulfide exchanges for 12 h at 37 °C. The products were purified with 20 mM Tris-HCl (pH 8.2) and concentrated to ~3 μM and ~10 μM using 10 K Amicon centrifugal filter (Millipore). The DNA handles were stored at 4 °C.

To form SNARE complexes, a 500 μl 1:1:1 mixture of syntaxin-1A, SNAP-25 and VAMP2 was incubated for 1 h at room temperature, with 10 mM DTT for reducing possible disulfide bonds and with 30 U/ml thrombin for the cleavage of 6xHis-tags. Following the cleavage, protease activity was inhibited by adding 2 mM AEBSF. The SNARE complexes were purified with 20 mM Tris-HCl (pH 8.2) using a PD MiniTrap G-25 desalting column (GE Healthcare) and concentrated to ~30 μM using 10 K Amicon centrifugal filter at 4 °C (fig. S10B).

To ensure the maximum likelihood of two different handles attaching to each SNARE complex, the handles were attached sequentially (*35*). First, about twentyfold excess of SNARE complex was reacted with biotin-modified DNA handle for 30 min at room temperature. Repetitive buffer exchanges were performed with 100 K Amicon centrifugal filter (Millipore). Then the SNARE complex attached to the biotin-modified handle was reacted with about twentyfold digoxigenin-modified DNA handle with 500 mM NaCl for 3 h at room temperature. The SNARE complex covalently linked to the respective DNA handles (SNARE-DNA hybrid) was analyzed by 6 % SDS-PAGE stained with SYBR Safe DNA Gel Stain (Invitrogen) (fig. S10C). The SNARE-DNA hybrid sample was stored at -80 °C with 10% glycerol added.

Magnetic tweezers experiment.

Single-molecule magnetic tweezers were built on an inverted microscope (Olympus, IX73) as previously described (*4, 27, 49-53*) and a microfluidic system for introducing proteins into the tweezers-chamber was connected (fig. S9A). Force calibrations for 1 μm and 2.8 μm magnetic beads (Invitrogen) are shown in fig. S9, B and C. A constant magnetic force of 3.9 pN (clamping-force) was applied to the SNARE

complex as the 'force-clamp' scheme to suppress thermal noise and then α-SNAP and NSF were sequentially introduced into the sample channel of the chamber (Fig. 3, A to C, and fig. S11). We used the 1 μm magnetic bead favorable for the force-clamp experiment, since at the same force the spatial resolution δx is better due to the smaller size of a bead when the measurement bandwidth Δf is below the roll-off frequency of power spectral density (*49, 54, 55*), by the equation

$$\delta x = \frac{\sqrt{4k_B T(\Gamma \eta R)\Delta f}}{k_{\text{trap}}}, \quad (1)$$

where $k_{\text{B}}T$ is the thermal energy, Γ the viscous drag coefficient, η the viscosity of the solution, R the radius of a bead and k_{trap} the trap stiffness. The imaging room of magnetic tweezers was maintained at constant temperature and humidity, and the sample chamber was maintained at 37 °C by a temperature-controlled holder. We injected buffers at a constant flow rate using the microfluidic system composed of a syringe pump (KD Scientific), syringe, tubing and needle (fig. S9A and see the upper right inset). The tubing and the syringe were entirely filled with the background buffer to reduce the measurement dead-time during injection. The background buffer was 50 mM HEPES-NaOH (pH 7.4) with 150 mM NaCl, 1-2 mM ATP, 10 mM Mg^{2+}, and 0.1 % Tween 20. The buffers containing proteins are of the same salt concentration and the same temperature as the background buffer, for maintaining the extension to be constant before and after the injection. The microscope stage drift of the magnetic bead is corrected every 500 ms by non-magnetic reference beads immobilized directly on the bottom surface. All extension traces obtained in the force-clamp experiments were median-filtered with 500 ms time-window.

For the negative-control experiment, we injected only the background buffer without any proteins (fig. S11). The Gaussian-peak differences before and after injection for each traces were plotted, with the analysis time fixed as 10 s (before injection) and 30 s (after injection) (less than the analysis-time scales in the main α-SNAP/NSF experiments). Averaging the peak differences at every time-window by finding the peak differences of the summed extension distributions (n=10), the extension level before and after the injection turned out to be maintained constant, below 0.3 nm. This result is well matched with the error-estimation (σ= 0.29 nm) by

$$\sigma = \sqrt{\frac{\sigma_i^2}{N_i} + \frac{\sigma_f^2}{N_f}}, \quad (2)$$

where σ is the standard error of the Gaussian-peak difference before and after injection, (σ_i, σ_f) the standard deviations of the respective extension traces, (N_i, N_f) the numbers of analyzed data points (*56*). The standard error σ was calculated as 0.29 nm when $\sigma_i = \sigma_f = 5$

nm (larger than typical standard deviation at 3.9 pN) and $N_i = N_f = 600$ (10 s for our 60 Hz CCD). Also, upon background buffer injection, the extension distribution broadened only ~0.3 nm (inset of fig. S11B). Thus the extension is stably maintained with a difference of only 3 Å for 8 minutes even buffer exchange is applied. This indicates that when a difference in the extension is measured, it likely reflects disassembly or reassembly induced in the SNARE complex.

To quantitatively analyze the magnitudes of destabilizations by α-SNAP and α-SNAP/NSF complex, we examined extensions as relative frequency (same as the analysis in the negative-control experiment), for the regions before and after α-SNAP injection and after NSF injection (Fig. 3D, n=23). While pulling a single SNARE complex with 3.9 pN force, we introduced α-SNAP and NSF in a sequential way (Fig. 3, A to C). When α-SNAP was injected, a small but significant increase of the extension was observed, consistent with the single-molecule FRET data suggesting that α-SNAP induces C-terminal destabilization of the SNARE complex (Fig. 3, A to C, blue versus red traces). For only single SNARE complexes without NSF and α-SNAP, the peak of the extension distribution is placed at 0 nm (Fig. 3D, blue distribution). This peak is shifted to 2.4($\pm$ 0.6) nm upon addition of α-SNAP (Fig. 3D, red distribution). With the worm-like chain model, this increase in the extension corresponds to destabilization up to the +8 layer at the C-terminal end of the SNARE motif (Fig. 3E, red distribution and table S1). Upon NSF addition, the extension was largely maintained as well at the same level until disassembly event, although the distribution became broader and the extension peak was slightly increased by 1 nm (Fig. 3, D and E, green distributions). The Gaussian-peak shifts could be assessed with ~0.3 nm accuracy obtained from the result of the negative-control experiment. The errors of the destabilizations were calculated as the further broadening of the extension distribution after protein injection, that is, the differences between standard deviations (SD) of the extension distributions minus 0.27 nm (SD of green or red histogram – SD of blue histogram – 0.27 nm). In this error estimation, we subtracted the value of 0.27 nm, as the average broadening only after background buffer injection. The destabilization error values are indicated in the parentheses below the peak values in Fig. 3D.

The magnitude of disassembly by NSF was determined as the difference between the arithmetic mean values of the respective extension traces (fig. S15A, blue and pink traces; n=10). For the differentiation analysis in fig. S15B, we median-filtered the extension traces before and after the disassembly signals (with 84 ms time-window) and smoothed the noise outside the signals (with 334 ms time-window), and then finally differentiated the signal-processed traces. Each derivative traces from 10 molecules were shifted to zero time and then averaged. We assessed the rate of the SNARE complex disassembly as the full width at half maximum (FWHM) of the fitted Gaussian function for the averaged derivative trace (fig. S15B, n=10). The errors of the disassembly rate were calculated as FWHMs of the fitted Gaussian functions for the standard-deviated derivative traces from the averaged one. The error values are indicated in parenthesis in fig. S15B.

The unzipping force of the SNARE complex.

In the magnetic tweezers experiments we apply 3.9 pN force to suppress thermal noise at 37 °C. The clamping-force of 3.9 pN has to be far below the unzipping force of the SNARE complex. Hence we checked how much force a SNARE complex can tolerate. To this end, we covalently knotted the N-terminal end of a SNARE complex in order to repeat the unzipping and rezipping for one molecule (fig. S13, A to C). Magnetic force cycles between 0 and 20 pN were repeated for several molecules ('force-ramp' scheme) (fig. S13A), during which the SNARE complexes were unzipped and rezipped appearing as stepwise increase and decrease of the extension (fig. S13D). The force-extension traces were median-filtered with 117 ms time-window. The measured unzipping and rezipping force distributions show that the most probable unzipping and rezipping forces are positioned at respectively 14.8 pN and 5.3 pN (fig. S13E, N =22). The standard deviations (SD) were each 2.8 pN and 1.5 pN. Therefore, the clamping-force of 3.9 pN is far below the 14.8 pN, the most probable unzipping force of a SNARE complex. The absolute value of force-(un)loading rate was less than 0.9 pN/s which can be considered as near equilibrium (*57*).

We have one more checkpoint on how long a SNARE complex tolerates the 3.9 pN force. To this end, we derived the equation for obtaining an unzipping rate constant at a certain force from the force-ramp experiment. For the unzipping force distribution $P(f)$, we can apply the following differentiation,

$$\left.\frac{dP(f)}{df}\right|_{f=f^*} = 0 \quad , \tag{3}$$

where f^* is the most probable unzipping force. Using the relation between the unzipping force distribution $P(f)$ and the survival probability $S(f)$ at the zipped state (*58*),

$$P(f) = -\frac{dS(f)}{df} = k(f)S(f) / \dot{f} \quad , \tag{4}$$

where $k(f)$ is the unzipping rate constant. Then *eq*. (3) is developed as,

$$\left.\frac{dP(f)}{df}\right|_{f=f^*} = \left[\frac{d}{df}\left(\frac{1}{\dot{f}}\right)kS + \frac{1}{\dot{f}}\left(\frac{dk}{df}S + k\frac{dS}{df}\right)\right]_{f=f^*} \tag{5}$$

$$= \left[\left(-\frac{1}{f} + \frac{x^\dagger}{k_BT} - \frac{k}{\alpha f}\right)\frac{kS}{\alpha f}\right]_{f=f^*} \tag{6}$$

$$= \frac{1}{f^*} - \frac{x^\dagger}{k_BT} + \frac{k_0 \exp(f^* x^\dagger / k_BT)}{\alpha f^*} = 0 \quad , \tag{7}$$

where k_0 is the unzipping kinetic rate at zero force and $x^\dagger$ is the distance from the zipped state to the transition state (from Bell's equation $k(f) = k_0 \exp(fx^\dagger / k_BT)$), and α is the

proportional constant of $\dot{f} = \dot{f}(f) = \alpha f$. The proportional constant α is obtained from the force calibration of the magnetic tweezers and the magnet speed in the force-ramp experiment. Inserting Bell's equation into *eq.* (7) to eliminate $x^{\dagger}$, the final equation is obtained as

$$\frac{1}{f^*} - \frac{1}{f}\ln\left(\frac{k(f)}{k_0}\right) + \frac{k_0}{\alpha f^*}\left(\frac{k(f)}{k_0}\right)^{\frac{f^*}{f}} = 0. \quad (8)$$

Using this formula, we obtained $k(f^*)$ = 0.3352 s^{-1} at f^* = 14.84 pN and $k(f_{clamp})$ = 1.1635x10^{-13} s^{-1} at $f_{clamp} = 3.9$ pN, with $\alpha = 0.0423$ s^{-1} and $k_0 = 4.2\text{x}10^{-18}$ s^{-1} (*59*). Therefore SNARE complexes are very unlikely to be unfolded at 3.9 pN during our experimental time of a few minutes.

Tension under hydrodynamic flow.

The tension applied to a SNARE complex is equal to the magnetic force when there is no flow. However, during injection of buffers into the sample channel, the tension is slightly increased due to hydrodynamic flow (*60-62*) (fig. S12A). Even during the flow, the mechanical tension applied to a SNARE complex should be below the unzipping force of SNARE complex. Thus we estimated the changes in tension when buffer flows in the channel. Since the global Reynolds number at 5 μl/s flow rate in the parallel plates (5 mm width and 76.2 μm thickness) is calculated as 2.87 (at 37 ℃), which is less than 10, the buffer flow can be assumed to be laminar flow. Then the velocity profile inside the parallel plates is,

$$v = \frac{3Q}{4wt^3}(t^2 - d^2), \quad (9)$$

where Q is the flow rate, w the width of the channel, t the half of the channel thickness, and d the distance from the virtual plane at the half of the channel thickness to the magnetic bead. With the velocity at the position of the 1 μm magnetic bead calculated by the velocity profile of *eq.* (9), the local Reynolds number at that position is estimated as 1.25×10^{-3}, which is much smaller than 1. Therefore Stokes' law can be applied,

$$F_d = 6\pi\mu R v, \quad (10)$$

where F_d is the hydrodynamic force, μ the dynamic viscosity, R the radius of the magnetic bead and v the relative velocity of the bead to the flow. Then the tension F_l is derived as,

$$F_l = F_d \sin\theta + F_m \cos\theta \quad (11)$$

$$= 6\pi\mu R v \sin\theta + F_m \cos\theta \quad (12)$$

$$= 6\pi\mu R \frac{3Q}{4wt^3}(t^2 - d^2)\sin\theta + F_m \cos\theta \quad (13)$$

$$= 6\pi\mu R\frac{3Q}{4wt^3}(t^2-(t-(R+l)\cos\theta)^2)\sin\theta + F_m\cos\theta \quad , \qquad (14)$$

where F_m is the magnetic force, θ the angle of the bead deflection during flow and l the DNA extension. In the calculation of the tension using *eq.* (14), the extension l varies with tension following the worm-like chain model (at the low force regime),

$$F_l = \left(\frac{k_BT}{P_d}\right)\left(\frac{1}{4(1-l/L_d)^2}-\frac{1}{4}+\frac{l}{L_d}\right) \quad , \qquad (15)$$

where k_BT is the thermal energy (= 4.28 pN·nm at 37 ℃), L_d the contour length of DNA calculated as the number of 1024 base pairs times 0.34 nm (*63*) and P_d the persistence length of 30 nm for DNA, typical at this contour length (*64*). By numerically solving *eq.* (14) and (15), we obtained the tension F_l with the angle of the bead deflection θ (fig. S12B).

The error of the tension was estimated by error propagation as $\sigma_{F_l} = \sqrt{(\sigma_{F_d}\sin\theta)^2 + (\sigma_{F_m}\cos\theta)^2}$ with $\sigma_{F_d} \approx (9\pi\mu RQ(R+l)\cos\theta / w^2t^4)\sqrt{(t^2\sigma_w)^2 + 2(wt\sigma_t)^2}$ from $\sigma_w, \sigma_t >> \sigma_R, \sigma_Q$ (σ_R = 0.03 R, σ_Q = 0.005 Q , σ_w = 0.2 w and σ_t = 0.1 t from product manuals) and with σ_{F_m} = 0.117 F_m at 3.9 pN clamping-force from the force calibration. Hence, at flow rates below 5 μl/s (the maximum rate used), the undesirable unzipping event of a SNARE complex solely by buffer flow can be assumed to be very unlikely, as the maximum possible tension of 7 pN during the flow is much less than 14.8 pN the most probable unzipping force of a SNARE complex.

Estimation on SNARE-complex extension.

In the previous forced unfolding studies of a SNARE complex, the experiment results match well with the structural model that when a SNARE complex is unzipped, VAMP2 becomes unstructured and the motif of the precomplex preserves its α-helical structure (*4, 5*). However, because the structural effects by α-SNAP and NSF could be different from simple unzipping by force, we analyzed the extension values for the two different models as the two extreme cases: 1) VAMP2 is unstructured and the precomplex preserves its α-helical structure [same as the earlier studies (*4, 5*)] or 2) both are unstructured. For the unstructured part, the extension l_p stretched by tension F_l was calculated by the worm-like chain model

$$\frac{F_lP_p}{k_BT} = \frac{1}{4}\left(1-\frac{l_p}{L_p}\right)^{-2} - \frac{1}{4} + \frac{l_p}{L_p} \quad , \qquad (16)$$

where $k_{\mathrm{B}}T$ is the thermal energy (= 4.28 pN·nm at 37 ℃), L_p the contour length calculated as the number of unzipped residues times 0.38 nm (*37*) and P_{p} the persistence length of 0.7 nm for the protein (*36, 65*). For the structured part, the extension was estimated as the layer-to-layer distance measured from the crystal structure of a SNARE complex (*3, 66*). For the first model, when the SNARE complex is unzipped more than the linker domains, the precomplex and VAMP2 should be aligned along the axial direction by the torque generated from the elastic rigidity of the precomplex (*4, 5*). In that case, 1.294 nm, which is the distance between the C-terminal DNA anchor residues, was subtracted from the total extension (*37, 67*). Consequently, when the clamping-force was 3.9 pN, the extension differences between the two models turned out to be all smaller than 1.2 nm (table S1). Thus, although exact structural states just after destabilization by α-SNAP and disassembly by NSF are hard to identify, the magnitudes of their effects can be described as precisely as ~1 layer accuracy independent of the models (Fig. 3E).

Supplementary Text

α-SNAP mediated destabilization of the C-terminal SNARE complex

To observe α-SNAP's effect, after taking single-molecule FRET images of SNARE complexes (with a FRET pair at either the C- or N- terminal, Fig. 2A and fig. S3), we injected α-SNAP and incubated for 3 min. After removing free molecules, we imaged single-molecule FRET signals from the SNAP-SNARE complexes. When α-SNAP was added to the labeled SNARE complexes, the FRET efficiency measured at the C-terminal end of the SNARE complex ($E_{\text{C-term}}$) significantly decreased (fig. S4, A to C). On the other hand, the FRET efficiency measured at the N-terminal end ($E_{\text{N-term}}$) remained invariant upon addition of α-SNAP (fig. S4D). Our observations suggest that α-SNAP addition induces selective destabilization in the C-terminal part of the SNARE complex while leaving the N-terminal intact.

We examined whether the observed decrease in the C-terminal FRET efficiency had a photophysical origin. To this end, we measured the changes in the quantum yield of the Cy3 and Cy5 dyes upon binding of the α-SNAP proteins. To measure these changes in an unambiguous way, we used Cy3 or Cy5 one at a time (fig. S4, E to H). First, we placed Cy3 at the C-terminal end of the SNARE complex (position 82 of sVAMP2), and no Cy5 in SNAP-25. Binding of α-SNAP induced enhancement of fluorescence intensity by 40% (fig. S4E), indicating that the quantum yield is increased by the same factor. When Cy3 is placed in the N-terminal end of the SNARE complex (position 30 of sVAMP2), a similar fluorescence enhancement was observed upon α-SNAP binding (fig. S4F).

Subsequently we placed Cy5 at the C-terminal end (position 79 of SNAP-25 and no Cy3 labeling in sVAMP2) and changed the excitation wavelength to 633 nm. Notably, binding of α-SNAP induced 10% decrease of the Cy5 fluorescence intensity instead of any fluorescence enhancement (fig. S4G). When we moved the Cy5 position to the N-terminal end (position 27 of SNAP-25), we only observed a 5% decrease of the Cy5 fluorescence (fig. S4H).

Next, we tried to explain the observed FRET decrease (from 0.8 to 0.1) with pure photophysical origins. The FRET efficiency is given as $E = \frac{I_A}{I_A + I_D} = \frac{\eta_A I_A^0}{\eta_A I_A^0 + \eta_D I_D^0}$, where I_D and I_A are the measured intensities of donor and acceptor, I_D^0 and I_A^0 are the true intensities of donor and acceptor emission, and η_D and η_A are the detection efficiencies of donor and acceptor determined by the instruments used. Since $I_D^0 \propto \frac{k_r}{k_r + k_{nr} + k_{RET}}$ and $I_A^0 \propto \frac{\phi_A k_{RET}}{k_r + k_{nr} + k_{RET}}$ (k_r, k_{nr} and k_{RET} are the kinetic rates of radiative decay, non-radiative decay and resonant energy transfer), we obtain $\frac{I_D^0}{I_A^0} = \frac{k_r}{\phi_A k_{RET}}$, where ϕ_A is the quantum yield of the acceptor. By inserting this ratio into the equation for E, we obtain $E = \frac{1}{1 + \frac{\eta_D}{\eta_A}\frac{k_r}{\phi_A k_{RET}}}$ (*68*).

From the manufacturer's data of the EMCCD used in this work, the ratio of η_D/η_A is found to be almost 1. This indicates that $\frac{k_r}{\phi_A k_{RET}} = 0.25$ for the Cy3-Cy5 pair attached at the C-terminal end of the SNARE complex before binding of α-SNAP (E~0.8). Since we are assuming that the observed FRET change is exclusively due to photophysics, we insert the changes in the quantum yield measured above (fig. S4, E to H) into this equation. We observed that k_r increased by a factor of 1.4 (40% increase) but this is accompanied by the change in k_{RET} by the same factor (the resonance energy transfer is considered instantaneous and only the function of the distance between the donor and acceptor dyes). ϕ_A is measured to be decreased by 10%. This collectively gives a new $\frac{k_r}{\phi_A k_{RET}} \approx 0.28$ and finally "a modified E of 0.78", indicating that the putative change due to pure photophysical effects is too small (from 0.8 to 0.78) to explain the observed FRET decrease from 0.8 to 0.1.

Hence, we conclude that the decrease of the FRET efficiency measured at the C-terminal end ($E_{C\text{-term}}$) mainly results from selective destabilization of the corresponding part of the SNARE complex by α-SNAP.

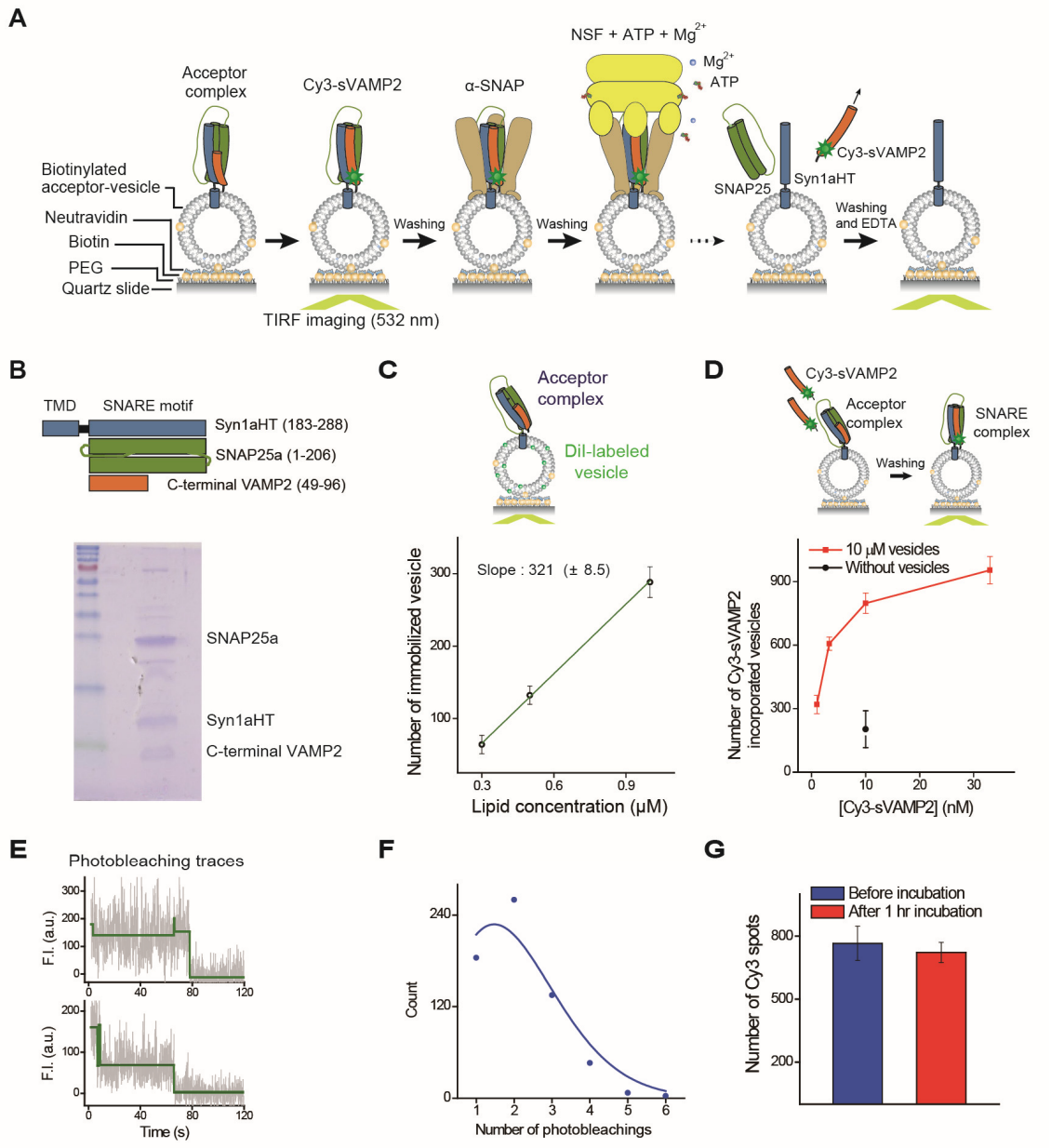

Fig. S1. Characterization of single-molecule fluorescence assay for SNARE-complex disassembly. (A) Experimental design. **(B)** SDS page gel of the acceptor complex stabilized by the C-terminal VAMP2 fragment (ΔN VAMP2 49-96). **(C)** Vesicle immobilization test. Vesicles labeled with 1 mol % DiI were excited with 532 nm laser (top). Count of surface-immobilized vesicles per imaging area (bottom) (n=40). The number of immobilized vesicles is linearly dependent on lipid concentration (i.e., vesicle concentration). The slope is 321±8.5 μM^{-1}. Lipid concentration of 10 μM was used for our main experiments, which gave about 3,000 immobilized vesicles per imaging area. **(D)** SNARE complex formation using unlabeled immobilized acceptor vesicles and Cy3-

sVAMP2. Number of SNARE complexes formed as a function of Cy3-sVAMP2 concentration when 10 μM vesicle was present (red) and when no acceptor vesicle was present (black) (*n*=40). **(E)** Representative photobleaching traces of Cy3-SNARE complexes in individual vesicles. A Schwarz information criterion was used to find steps (bold lines). **(F)** Distribution of the number of photobleaching steps in a vesicle (*n*=635). The data was fitted with a Poisson distribution. The average number is 2 ± 0.2 (s.e.m.). **(G)** Stability of the SNARE complex during our experiments. We compared the number of Cy3-sVAMP2 incorporated vesicles before and after incubating for an hour at 37℃.

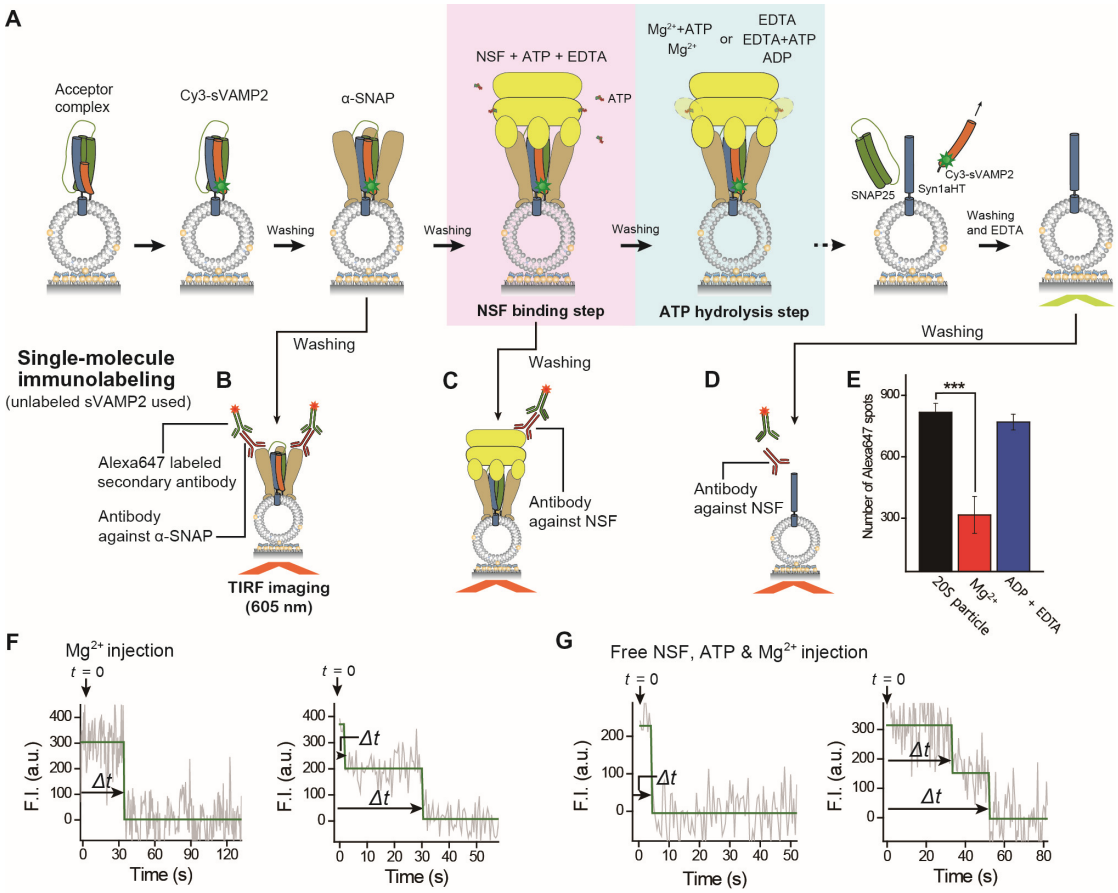

Fig. S2. Disassembly with one-round ATP hydrolysis during the disassembly reaction. **(A)** Experimental design. **(B to D)** Experimental design for single-molecule immunolabeling assays for confirmation of α-SNAP-binding (B), NSF-binding (C) and NSF release after ATP hydrolysis (D). **(E)** Number of Alexa647 spots measured after incubation with the depicted components of the disassembly reaction. **(F and G)** Representative real-time traces for disassembly involving only one-round of ATP hydrolysis (F) and in the presence of excess NSF, ATP, and Mg^{2+} (G). Grey shows the fluorescence intensity traces, and dark green denotes stepwise changes identified by a step finding algorithm.

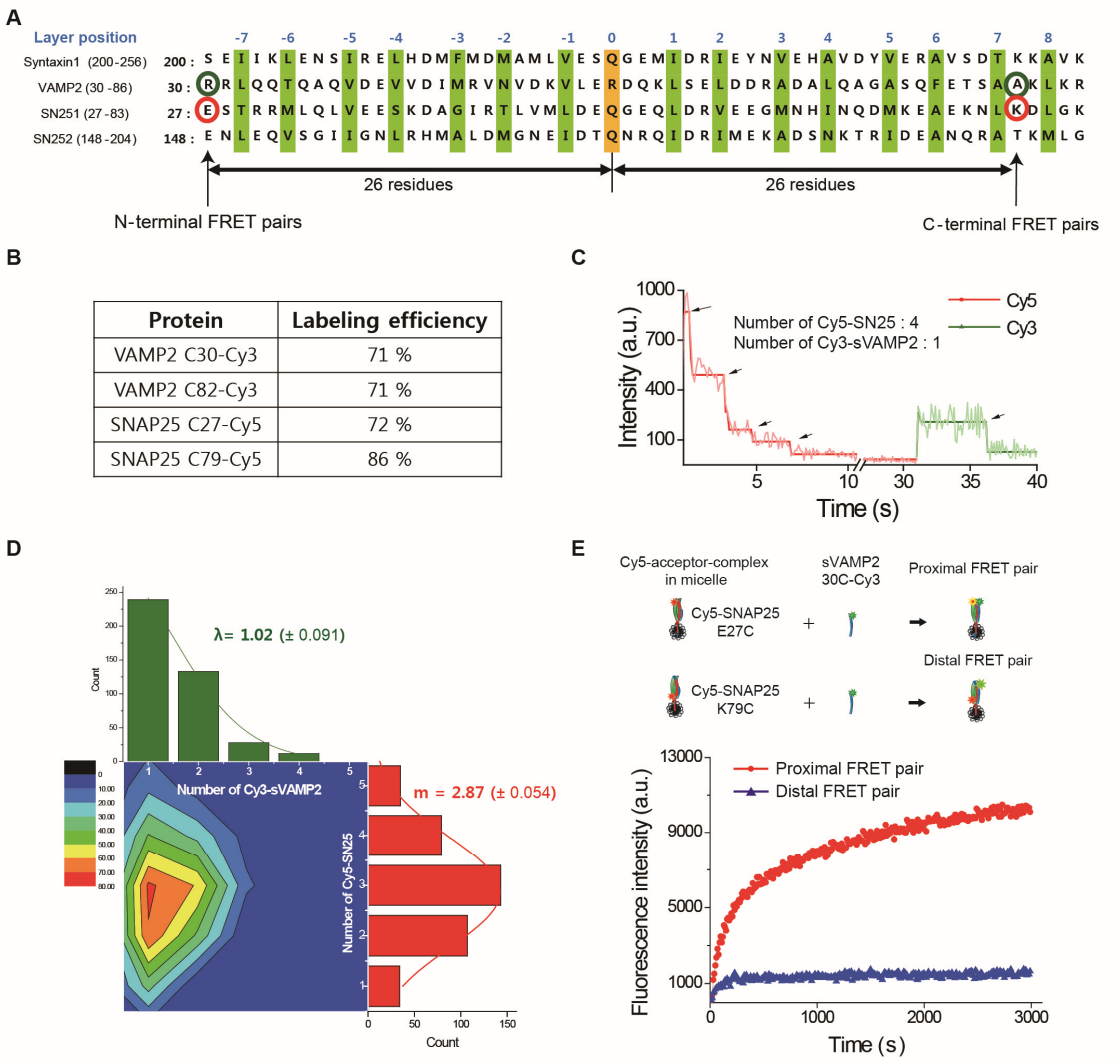

Fig. S3. Reconstitution of SNARE complexes in vesicles. (A) N- and C-terminal labeling positions in the SNARE complex. The distances from the 0th layer to the N- and C-terminal labeling sites are same (26 residues). **(B)** Labeling efficiency for each protein. **(C)** Representative trace from photobleaching experiments. From 0 to 32 sec, Cy5 dyes were bleached using a red laser (605 nm), and Cy3 dyes were bleached using a green laser (532 nm) from 32s. Thick lines are fitted traces with step locations determined using the Schwarz information criterion. **(D)** 2D distributions of the number of Cy3-sVAMP and Cy5-SNAP-25 incorporated in a vesicle. The average number of Cy3-sVAMP2 in a vesicle was 1.02±0.091 (n=412), and that of Cy5-SNAP-25 was 2.87±0.054 (s.e.m.). The number distribution of Cy3-sVAMP2 was fitted with a Poisson distribution and that of Cy5-SNAP-25 was fitted with a Gaussian distribution. The difference between the mean number of Cy3-sVAMP2 and Cy5-SNAP-25 is due to the orientation of Cy5-SNAP-25 and to the efficiency of SNARE complex formation. **(E)** Bulk FRET measurements from mixing

SNAREs labeled at the N- terminals and SNAREs labeled at the N- and C- terminals, in 1 % OG (Octyl β-D-glucopyranoside). The N-terminal FRET was measured by reaction of N-terminal labeled Cy3-sVAMP2 to N-terminal labeled Cy5-acceptor complex, while for the opposite-site FRET pairs C-terminal labeled Cy3-sVAMP2 was added instead.

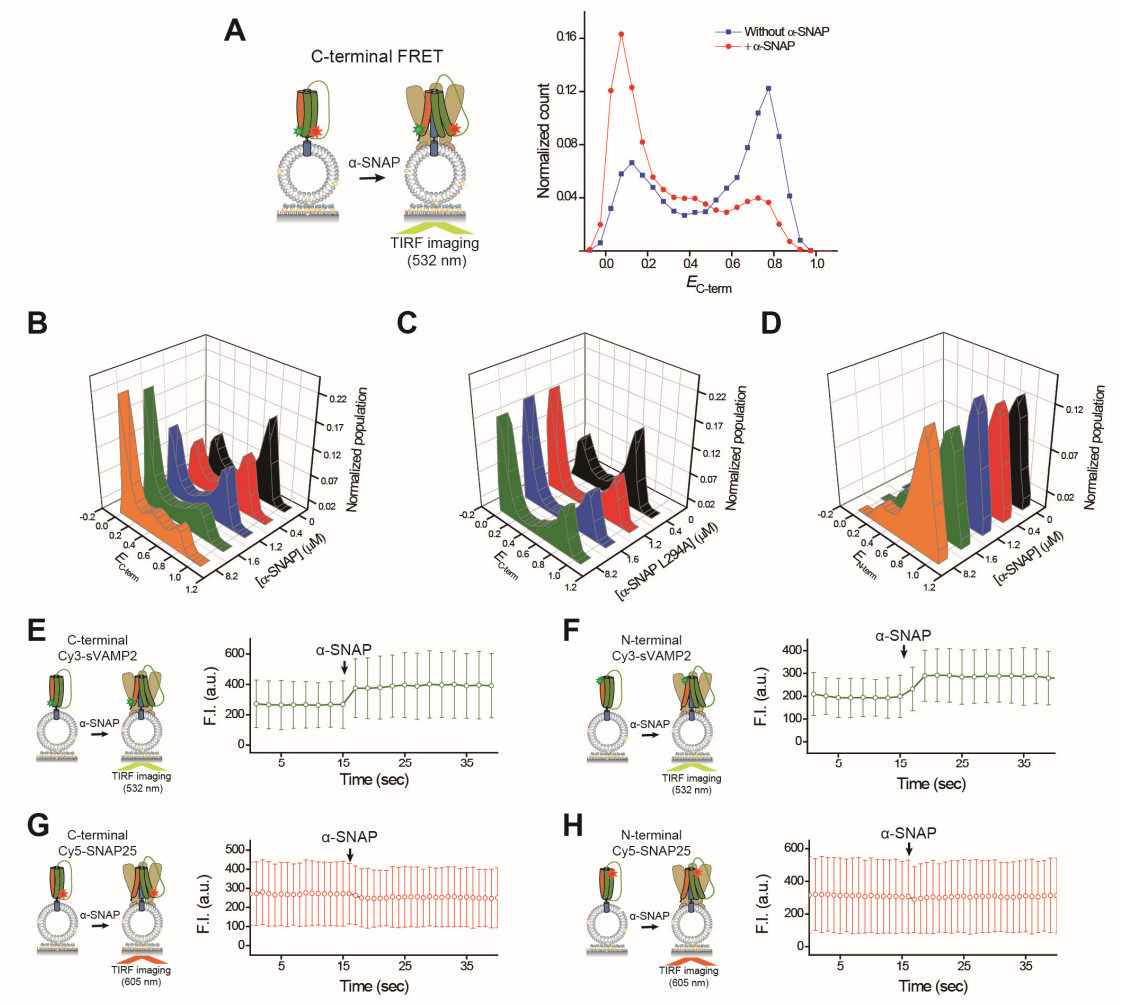

Fig. S4. α-SNAP induced selective destabilization of C-terminal SNARE complex. (A) Single-molecule FRET distributions measured for the C-terminal FRET pair with α-SNAP. **(B to D)** α-SNAP titration with single-molecule FRET distributions measured for the C-terminal FRET pair with α-SNAP (B), with α-SNAP L294A (C), and the N-terminal FRET pair (D) with varying α-SNAP concentrations from 0 to 16.3 μM. See Supplementary Text for detailed discussion. **(E to H)** Average fluorescence intensity traces for Cy3-labeled on C-terminal sVAMP2 (*n*=300) (E), and on N-terminal sVAMP2 (*n*=309) (F), and Cy5-labeled on C-terminal sVAMP2 (*n*=211) (G), and on N-terminal sVAMP2 (*n*=263) (H). α-SNAP was injected at 16 sec. Error bars are standard deviations.

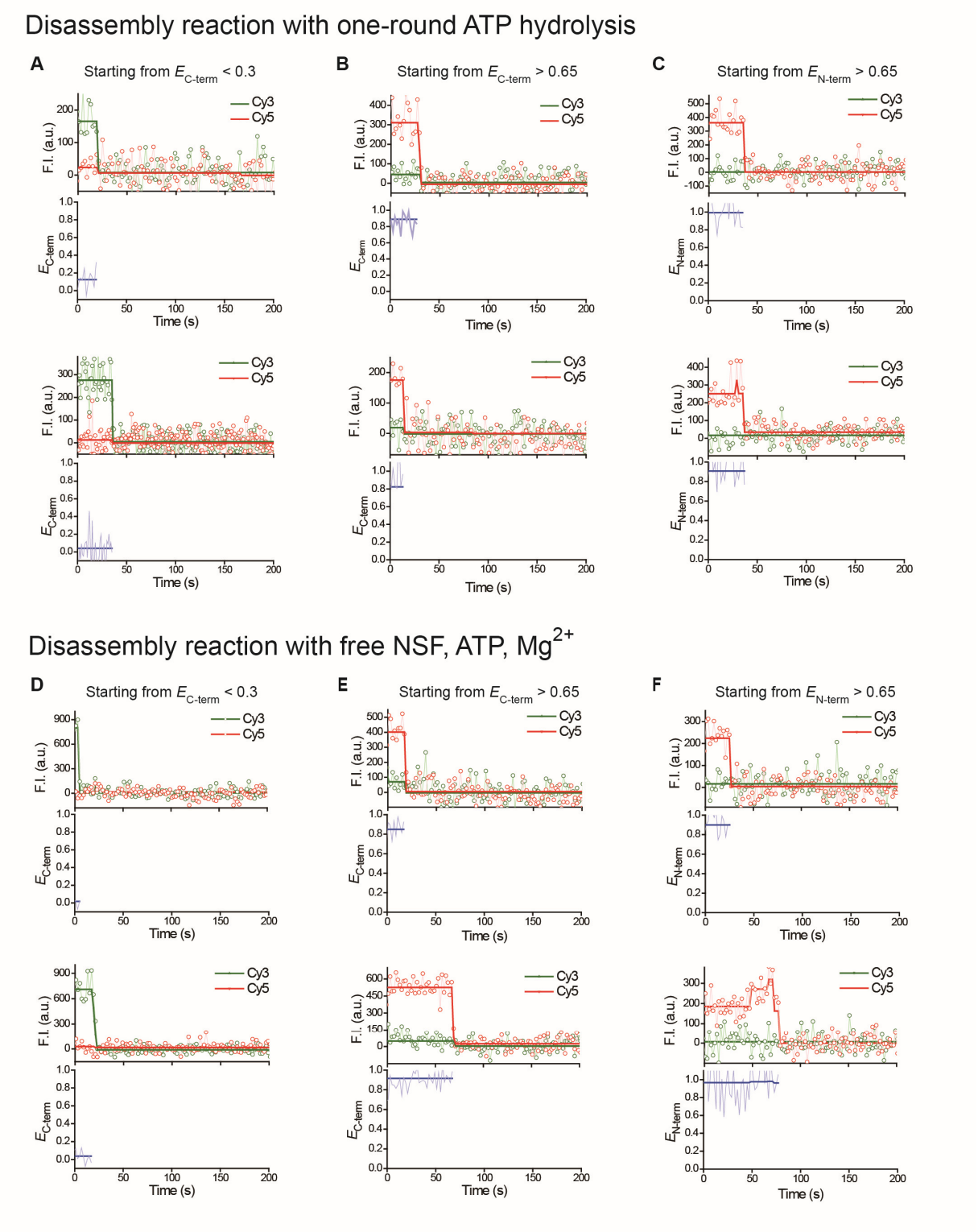

Fig. S5. Real-time traces for disassembly of single SNARE complexes monitored with single-molecule FRET. (A to C) Representative disassembly traces obtained with one

round of ATP hydrolysis. Traces starting from low FRET (<0.3) and (A) and starting from high FRET (>0.65) **(B)** where the SNARE complexes were labeled at the C-termini. Traces starting from high FRET (>0.65) where the SNARE complexes were labeled at the N-terminus (C). **(D to F)** Disassembly traces in the presence of excess NSF, ATP, and Mg^{2+}. Traces start either from low FRET (<0.3) (D) or from high FRET (>0.65) (E), where the SNARE complexes were labeled at the C-termini. Traces starting from high FRET (>0.65) where the SNARE complexes were labeled at the N-termini (F).

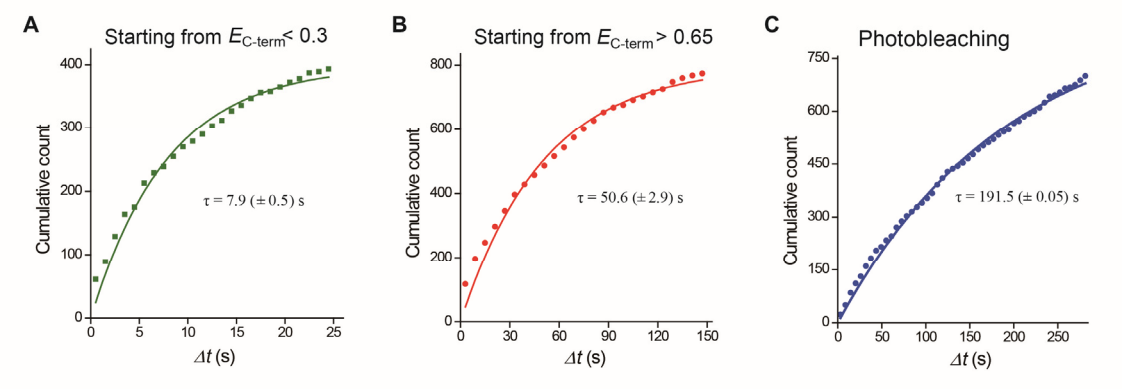

Fig. S6 Distributions of latency between Mg^{2+} injection and disassembly for complexes (A) starting at low FRET (*n*=393) **(B)** and high FRET (*n*=774). Real-time FRET disassembly assays were performed for both N-and C-terminally labeled SNARE complexes and for the two disassembly conditions**.** When the latency (*Δt* from Mg^{2+} injection to a disassembly event) distribution was plotted, it was well fitted with a single exponential function, indicating a single rate-limiting step during the disassembly reaction. The kinetic rate for disassembly is six times faster when the real-time trace started from the low $E_{C\text{-}term}$ state, indicating that the more destabilized the SNARE complex is (by α-SNAP), the faster the disassembly event occurs. **(C)** Photobleaching kinetics in our single-molecule FRET experiment. Cumulative distribution of latencies of photobleaching events in the presence of an imaging buffer, consisting of trolox and an oxygen-scavenging system. Fitting was done using a single-exponential function. τ is the time constant with the s.e.m.

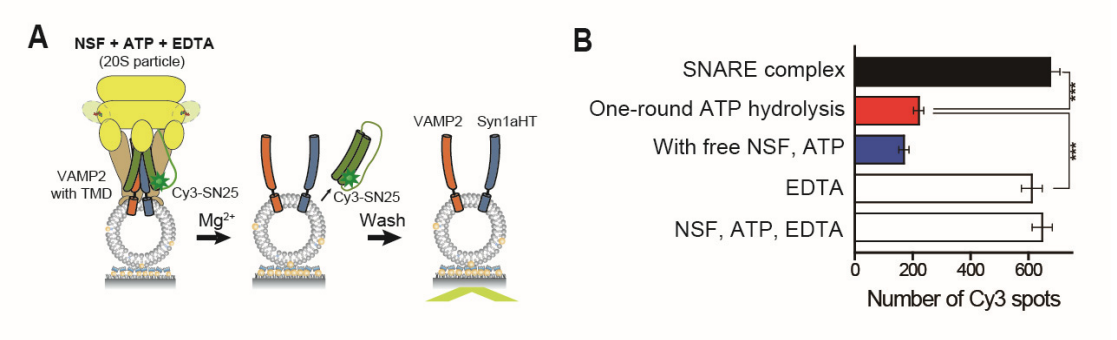

Fig. S7 SNAP-25 dissociation from the SNARE complex with two transmembrane domains. (A) Experimental design. We reconstituted full-length VAMP2 together with the acceptor complex (with Cy3 labeled SNAP-25) in vesicles to test whether NSF can disassemble SNARE complexes with one-round ATP turnover in their native configuration. **(B)** Number of Cy3 spots after disassembly. SNAP-25 was found to dissociate upon disassembly with one-round ATP turunover.

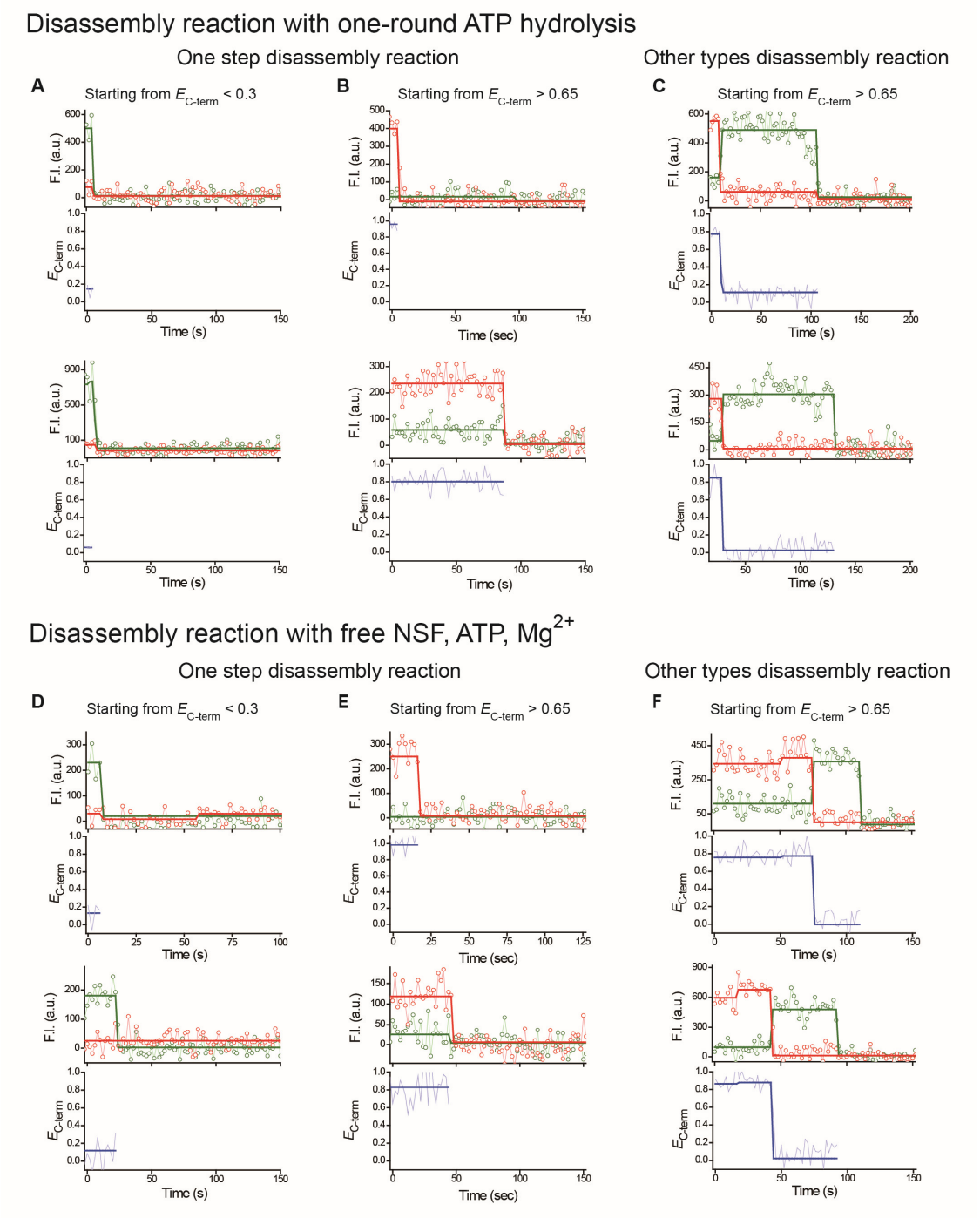

Fig. S8. Real-time smFRET traces for disassembly of single SNARE complexes with two TMDs. (A to C) Representative disassembly traces for disassembly with one-round ATP hydrolysis. One-step disassembly starting from low FRET ($E_{C\text{-}term}$<0.3) (A) and starting from high FRET ($E_{C\text{-}term}$>0.65) (B). Other types of disassembly starting from high FRET ($E_{C\text{-}term}$>0.65) (C). **(D to F)** Representative disassembly traces for disassembly with

free NSF, and free ATP. One-step disassembly starting from low FRET ($E_{C\text{-}term}$<0.3) (D) and starting from high FRET ($E_{C\text{-}term}$>0.65) (E). Other types of disassembly starting from high FRET ($E_{C\text{-}term}$>0.65) (F).

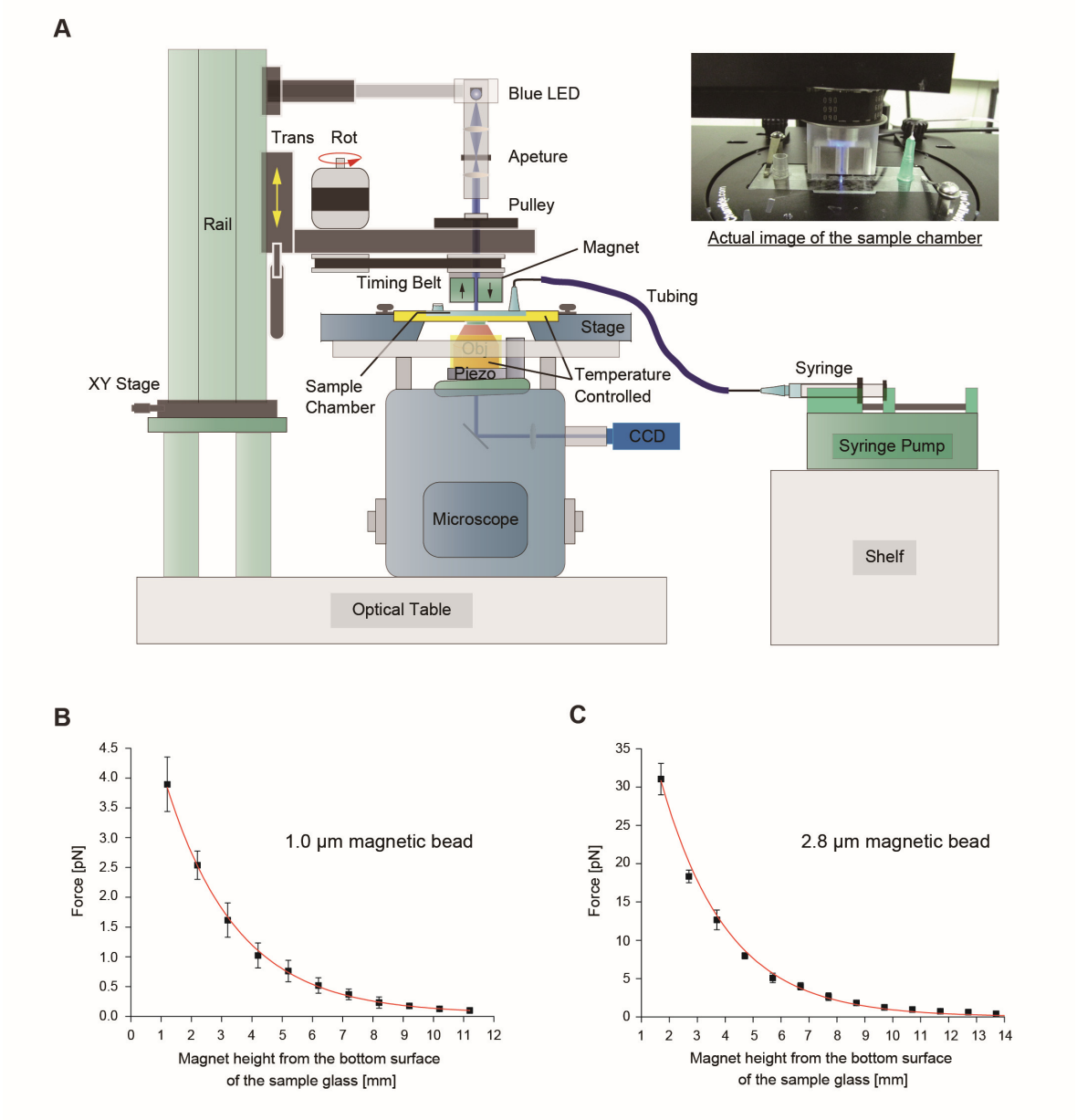

Fig. S9. Schematic of magnetic tweezers and force calibration data. (A) Schematic diagram for the magnetic tweezers with a microfluidic system composed of syringe pump, syringe, tubing and needle. The upper right inset shows the actual image of the fluidic sample chamber. The sample stage and objective lens are maintained at 37 ℃. The magnet position is controlled by translational and rotational motors. The magnetic beads are illuminated with a blue light emitting diode and imaged with a 60 Hz CCD. **(B and C)** Calibration of magnetic force versus magnet height for (B) 1.0 μm magnetic bead and (C) 2.8 μm magnetic bead. The 1.0 μm bead was used in the force-clamp experiment for studying NSF/α-SNAP-driven SNARE complex disassembly. The 2.8 μm bead, with

which we can apply force over 30 pN, was used in the force-ramp experiment for finding the most probable unzipping force of a SNARE complex. The force measurements are fitted with exponential functions.

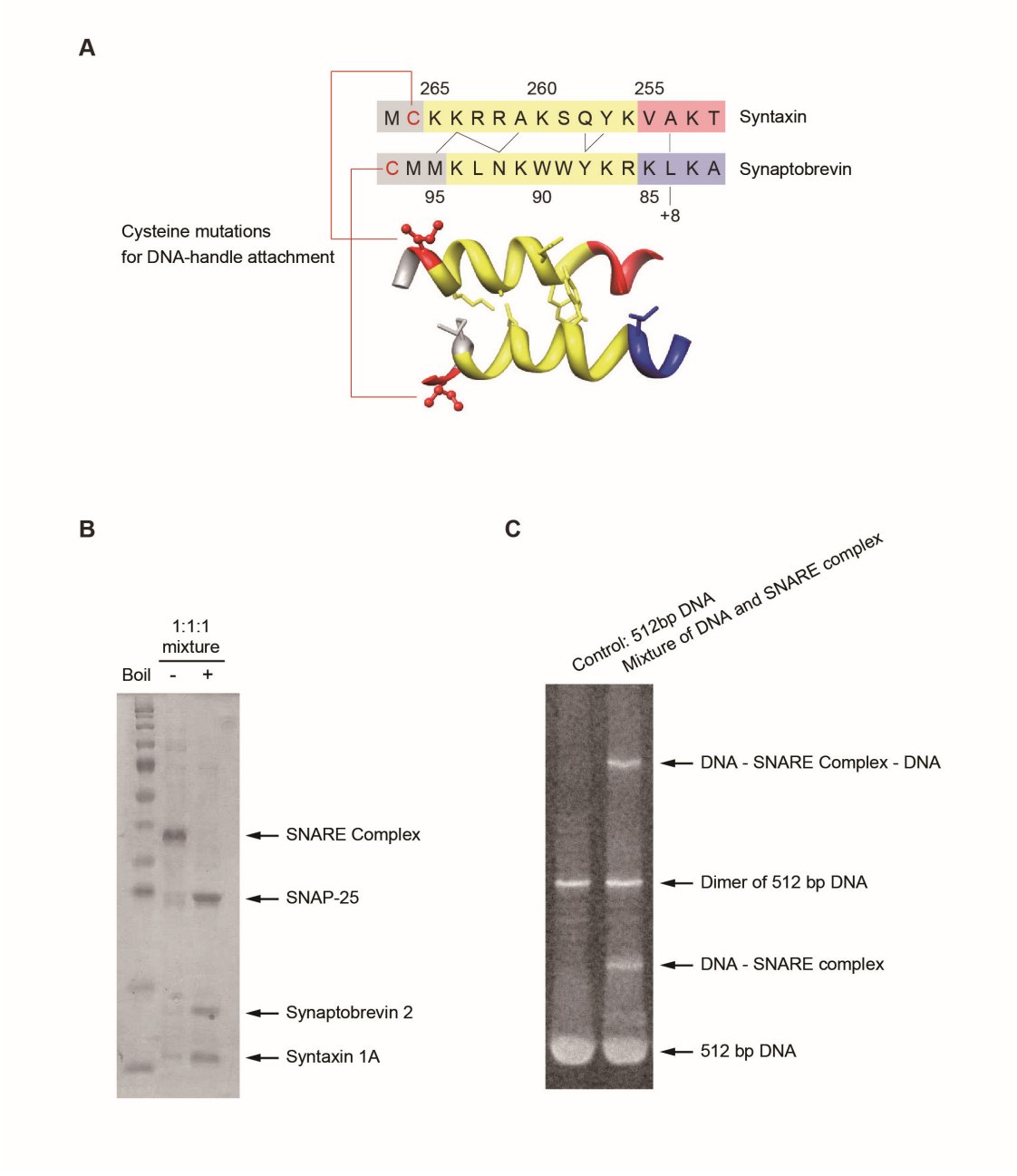

Fig. S10. Handle-attachment positions and gel analyses. (A) Amino acid sequences and structure diagram of the very C-terminal part of the SNARE complex. The selected residues protruding outside are replaced with cysteines in order to attach DNA handles by thiol-disulfide exchange reaction. **(B)** 12% SDS-PAGE confirming each SNARE protein and their assembly into a SNARE complex. **(C)** 6 % SDS-PAGE verifying the molecular construct of a SNARE complex linked to 512 bp DNA handles (stained with SYBR Safe DNA Gel Stain).

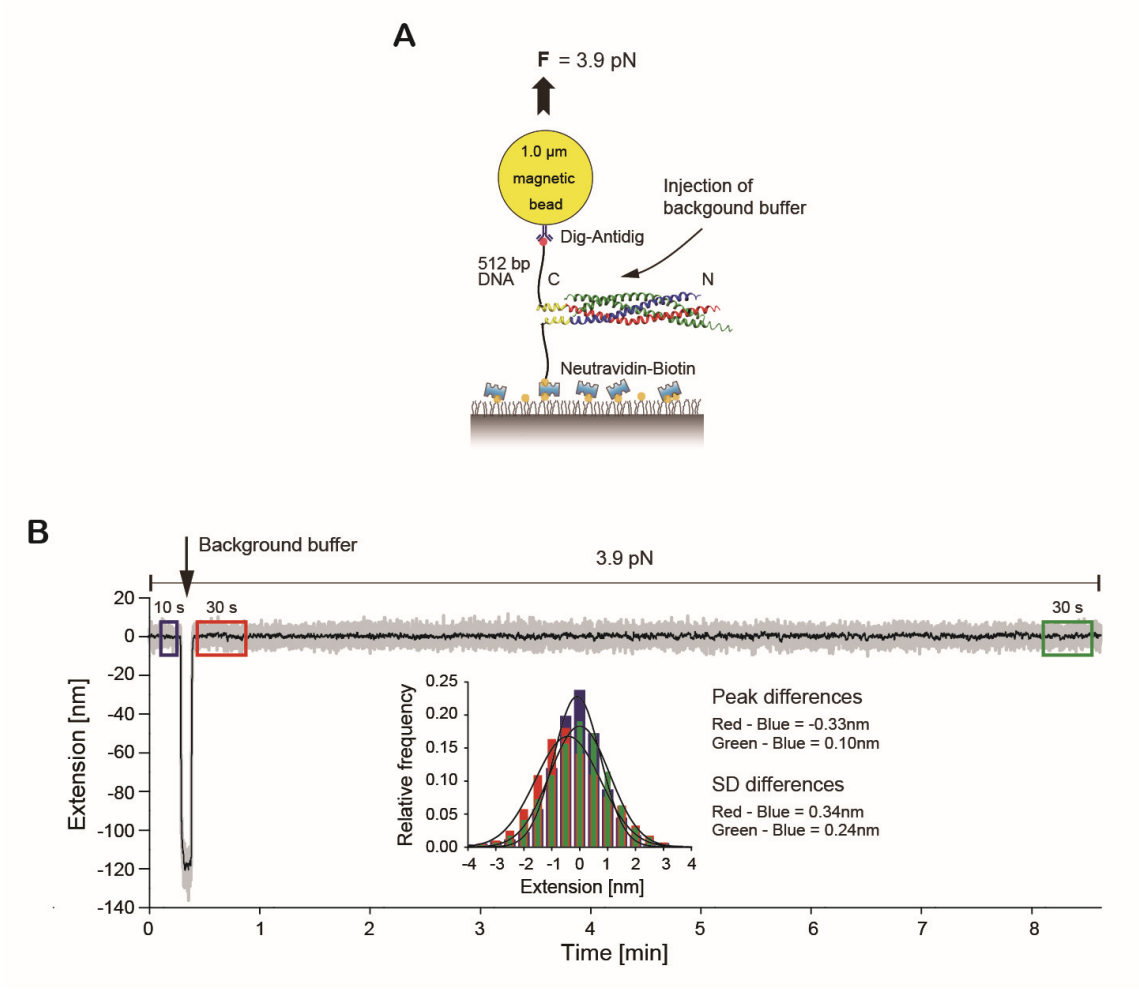

Fig. S11. Control experiment of buffer exchange. (A) Schematic diagram of the magnetic-tweezers experiment in which the background buffer exchange was applied. **(B)** Representative trace of the control experiment. Little extension change of the SNARE-DNA hybrid was observed over 8 min. Inset: Differences between the Gaussian peaks and standard deviations (SD) of the extension distributions before and after injection (n=10). See Materials and Methods for more details.

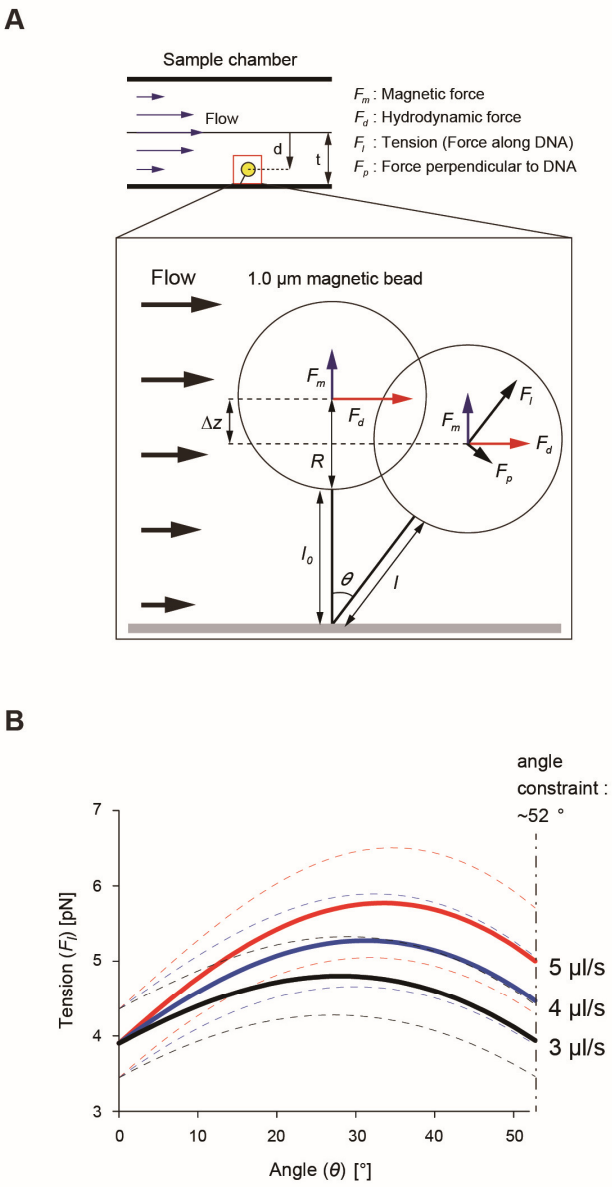

Fig. S12. Estimation of tension during hydrodynamic flow. (A) Schematic diagram showing the force components acting on a magnetic bead during hydrodynamic flow. The tension (= force along DNA) is numerically calculated using Stokes' law and the worm-like chain model. **(B)** Estimated tension as a function of the angle of bead deflection at 3, 4 and 5 μl/s flow rates (shown as black, blue and red solid lines). The errors of tension, shown as dashed lines, are estimated by error propagation. The angle constraint is the critical angle at which the magnetic bead hits the glass surface.

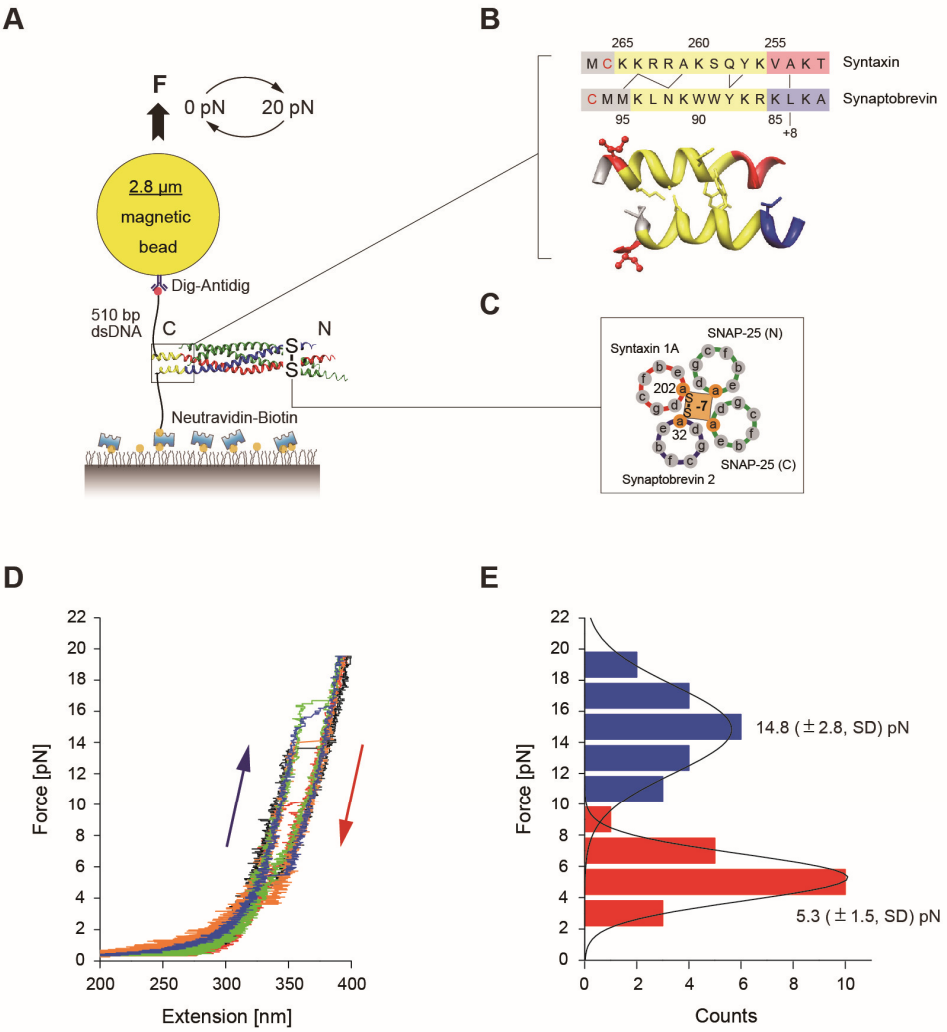

Fig. S13. Force-ramp experiment for finding the unzipping and rezipping forces. (A) Schematic diagram of the force-ramp experiment that examines the unzipping and rezipping forces of SNARE complexes. The magnetic force is cycled between 0 pN and 20 pN and the resultant force-extension curves are monitored. **(B)** Amino acid sequences and structure diagram at the very C-terminal part of a SNARE complex (same as fig. S10A). The selected residues protruding outside are replaced with cysteines in order to attach DNA handles by thiol-disulfide exchange reaction. **(C)** Helical wheel diagram in the N-terminal of a SNARE complex showing the disulfide bond at the -7 layer that makes repetitive unzipping and rezipping possible for one molecule. **(D)** Representative force-extension curves with stepwise extension changes corresponding to unzipping and rezipping events of SNARE complexes. The absolute values of force-loading and unloading rates are below 0.9 pN/s. **(E)** Unzipping and rezipping force distributions (shown as blue and red histograms, *N*=22). The most probable unzipping and rezipping forces are obtained as 14.8

pN and 5.3 pN by finding the peaks of the fitted Gaussian functions. The standard deviations (SD) are 2.8 pN and 1.5 pN, respectively.

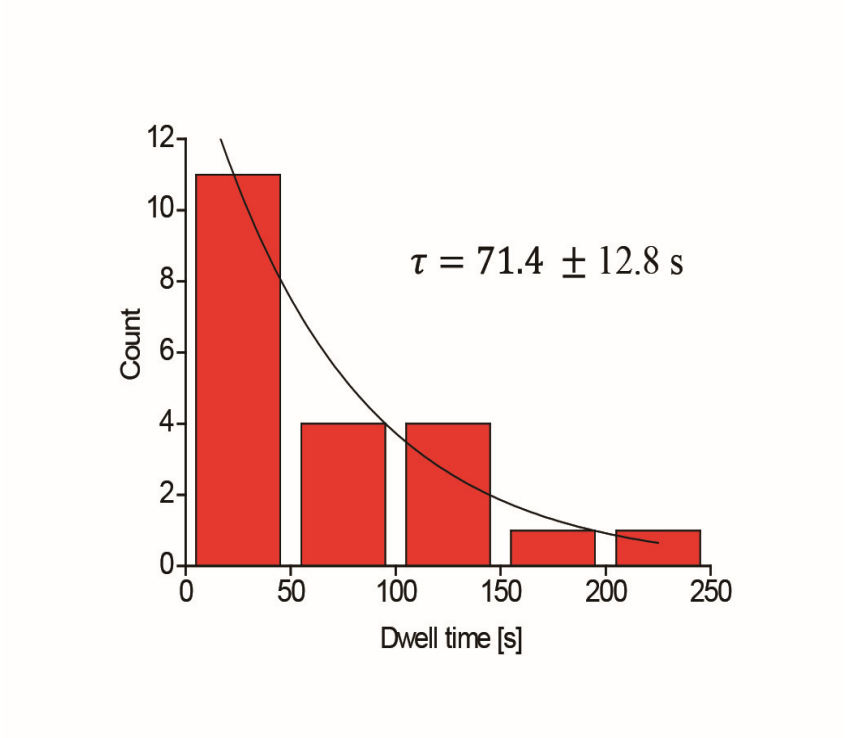

Fig. S14. Distribution of latencies from NSF, ATP, Mg^{2+} addition to final disassembly event during magnetic tweezing experiments. The time constant is 71.4 ± 12.8 s (s.e.m., *n*=21).

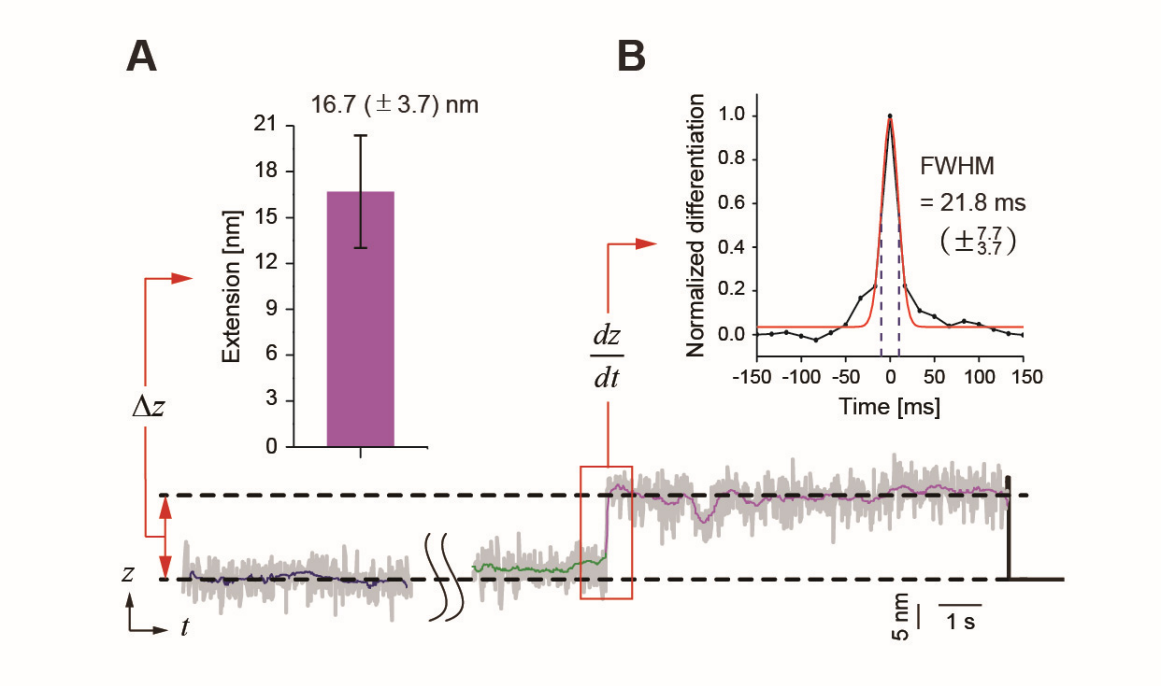

Fig. S15. Estimations of the disassembly size (A) and its rate (B). The average size of the extension burst was 16.7(±3.7) nm (A), corresponding to disassembly up to the -7 layer that is the N-terminal end of the SNARE motif (Fig. 3E, pink distributions). Moreover, the extension burst was completed within 21.8 ms (B).

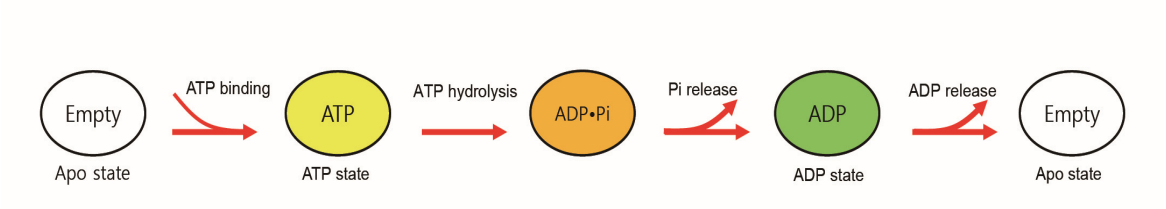

Fig. S16. The ATP hydrolysis cycle and the possible models of action of NSF. Our experimental observations can be summarized as 1) the NSF hexamer needs only one round of ATP hydrolysis to disassemble a single SNARE complex. 2) Before disassembly, there is a delay of up to tens of seconds that has one rate-limiting step. 3) The disassembly event itself is completed in a burst within 20 ms. These observations raise a question of where the bust disassembly is positioned in the given, single ATP hydrolysis cycle. ATP binding clearly precedes disassembly, as disassembly can be triggered by Mg^{2+} ions only once the 20S complex is formed (e.g., Fig. 1E). Furthermore, it is likely that disassembly precedes ADP release because large conformational changes have been observed between the ATP- and ADP-bound states (*11, 12*). This is further supported by the fact that addition of ADP to the 20S particles does not induce disassembly (see Fig. 1H). Moreover, as ring-type ATPases are thought to release only a small free energy at the moment of gamma phosphate cleavage, this step is unlikely to be the force generating step (*69*). In this vein, we are left with only two scenarios, where the disassembly event is tightly coupled to either Pi release or the ADP-bound state. These two scenarios are shown in Figure 4, F and G.

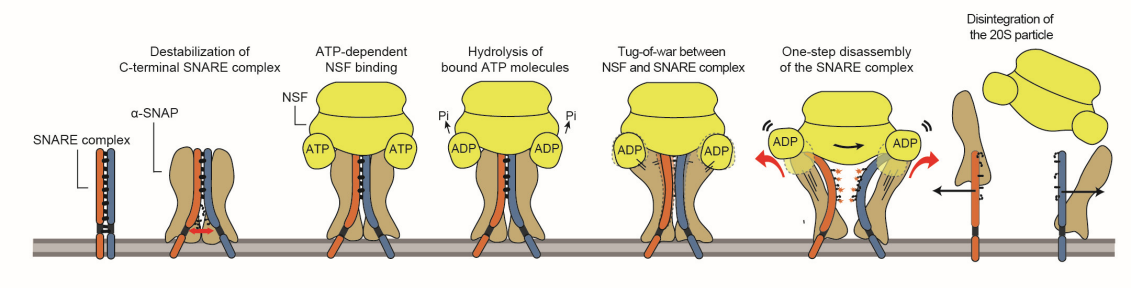

Fig. S17. Working model of the spring-loaded mechanism of NSF. When α-SNAPs bind to a single SNARE complex, partial destabilization is selectively induced in the C-terminal part of the SNARE complex. When NSF binds on top of this complex, hydrolysis of ATP bound to NSF is accelerated. Phosphate ions are released, and the NSF subunits try to switch to the ADP-bound conformation, involving a major movement of the N-domain to the peripheral side of the D1 domain. There is a mechanical force exerted on the SNARE complex that resists against disassembly while NSF tries to switch to the ADP state and release the tension. When there is a brief destabilization of the SNARE complex through thermal fluctuation, NSF disassembles the whole SNARE complex in one step. After disassembly, the individual SNARE proteins are immediately released with dissociation of the 20S particle. Recently, sub-nanometer to near-atomic resolution structures have been reported for the 20S complex by use of single-particle electron cryomicroscopy (*31*). While the new structure does not directly explain the disassembly mechanism, it seems to be compatible with the spring-loaded mechanism we report in this work. Considering breakdown of the symmetry due to the fact that six N-domains need to be aligned with four α-SNAPs, there appears to be different assemblies of the N-domains and α-SNAPs (*31*). These various "starting points" may be best compatible with a concerted, tension-based mechanism as it does not matter how exactly and in which topology NSF "pushes (or pulls)" the α-SNAPs as long as there is sufficient tension being generated.

Table S1. Extension values of a SNARE complex disassembled up to the hydrophobic layers. The expected extensions at 3.9 pN are estimated for the two structural models as a single SNARE complex is unzipped to specific layers from the DNA anchor positions. The extensions for a selected position in the linker domain are also shown, in which the amino acids form interaction with each other (*66*) (the uppermost row). The extension values as a SNARE complex is unzipped up to the structural end, are estimated as well (the bottom row). The notation (x,x) in the 'Layers' column denotes the positions of amino acid residues of syntaxin-1A (left) and VAMP2 (right).

Layers	Model 1 with α-helical precomplex structure [nm]	Model 2 with unfolded precomplex structure [nm]
(258, 88)	2.1	
+8	3.1	
+7	2.7	3.9
+6	3.8	4.9
+5	4.6	5.6
+4	5.7	6.7
+3	6.5	7.4
+2	7.5	8.4
+1	8.4	9.2
0	9.5	10.2
-1	10.3	10.9
-2	11.4	11.9
-3	12.2	12.7
-4	13.2	13.7
-5	14.1	14.4
-6	15.2	15.4
-7	16.0	16.2
(191, 21)	19.0	19.0

References

1. T. Söllner, S. W. Whiteheart, M. Brunner, H. Erdjument-Bromage, S. Geromanos, P. Tempst, J. E. Rothman, SNAP receptors implicated in vesicle targeting and fusion. *Nature* 362, 318–324 (1993). Medline doi:10.1038/362318a0

2. P. I. Hanson, R. Roth, H. Morisaki, R. Jahn, J. E. Heuser, Structure and conformational changes in NSF and its membrane receptor complexes visualized by quick-freeze/deep-etch electron microscopy. *Cell* 90, 523–535 (1997). Medline doi:10.1016/S0092-8674(00)80512-7

3. R. B. Sutton, D. Fasshauer, R. Jahn, A. T. Brunger, Crystal structure of a SNARE complex involved in synaptic exocytosis at 2.4 A resolution. *Nature* 395, 347–353 (1998). Medline doi:10.1038/26412

4. D. Min, K. Kim, C. Hyeon, Y. H. Cho, Y. K. Shin, T. Y. Yoon, Mechanical unzipping and rezipping of a single SNARE complex reveals hysteresis as a force-generating mechanism. *Nat. Commun.* 4, 1705 (2013). Medline doi:10.1038/ncomms2692

5. Y. Gao, S. Zorman, G. Gundersen, Z. Xi, L. Ma, G. Sirinakis, J. E. Rothman, Y. Zhang, Single reconstituted neuronal SNARE complexes zipper in three distinct stages. *Science* 337, 1340–1343 (2012). Medline

6. F. Li, F. Pincet, E. Perez, W. S. Eng, T. J. Melia, J. E. Rothman, D. Tareste, Energetics and dynamics of SNAREpin folding across lipid bilayers. *Nat. Struct. Mol. Biol.* 14, 890–896 (2007). Medline doi:10.1038/nsmb1310

7. D. W. Wilson, C. A. Wilcox, G. C. Flynn, E. Chen, W. J. Kuang, W. J. Henzel, M. R. Block, A. Ullrich, J. E. Rothman, A fusion protein required for vesicle-mediated transport in both mammalian cells and yeast. *Nature* 339, 355–359 (1989). Medline doi:10.1038/339355a0

8. S. W. Whiteheart, I. C. Griff, M. Brunner, D. O. Clary, T. Mayer, S. A. Buhrow, J. E. Rothman, SNAP family of NSF attachment proteins includes a brain-specific isoform. *Nature* 362, 353–355 (1993). Medline doi:10.1038/362353a0

9. T. Söllner, M. K. Bennett, S. W. Whiteheart, R. H. Scheller, J. E. Rothman, A protein assembly-disassembly pathway in vitro that may correspond to sequential steps of synaptic vesicle docking, activation, and fusion. *Cell* 75, 409–418 (1993). Medline doi:10.1016/0092-8674(93)90376-2

10. U. Winter, X. Chen, D. Fasshauer, A conserved membrane attachment site in alpha-SNAP facilitates N-ethylmaleimide-sensitive factor (NSF)-driven SNARE complex disassembly. *J. Biol. Chem.* 284, 31817–31826 (2009). Medline doi:10.1074/jbc.M109.045286

11. L. F. Chang, S. Chen, C. C. Liu, X. Pan, J. Jiang, X. C. Bai, X. Xie, H. W. Wang, S. F. Sui, Structural characterization of full-length NSF and 20S particles. *Nat. Struct. Mol. Biol.* 19, 268–275 (2012). Medline doi:10.1038/nsmb.2237

12. A. Moeller, C. Zhao, M. G. Fried, E. M. Wilson-Kubalek, B. Carragher, S. W. Whiteheart, Nucleotide-dependent conformational changes in the N-ethylmaleimide Sensitive Factor

(NSF) and their potential role in SNARE complex disassembly. *J. Struct. Biol.* 177, 335–343 (2012). Medline doi:10.1016/j.jsb.2011.12.018

13. C. U. Lenzen, D. Steinmann, S. W. Whiteheart, W. I. Weis, Crystal structure of the hexamerization domain of N-ethylmaleimide-sensitive fusion protein. *Cell* 94, 525–536 (1998). Medline doi:10.1016/S0092-8674(00)81593-7

14. R. C. Yu, P. I. Hanson, R. Jahn, A. T. Brünger, Structure of the ATP-dependent oligomerization domain of N-ethylmaleimide sensitive factor complexed with ATP. *Nat. Struct. Biol.* 5, 803–811 (1998). Medline doi:10.1038/1843

15. E. E. Nagiec, A. Bernstein, S. W. Whiteheart, Each domain of the N-ethylmaleimide-sensitive fusion protein contributes to its transport activity. *J. Biol. Chem.* 270, 29182–29188 (1995). Medline doi:10.1074/jbc.270.49.29182

16. C. Zhao, E. A. Matveeva, Q. Ren, S. W. Whiteheart, Dissecting the N-ethylmaleimide-sensitive factor: Required elements of the N and D1 domains. *J. Biol. Chem.* 285, 761–772 (2010). Medline doi:10.1074/jbc.M109.056739

17. M. E. Aubin-Tam, A. O. Olivares, R. T. Sauer, T. A. Baker, M. J. Lang, Single-molecule protein unfolding and translocation by an ATP-fueled proteolytic machine. *Cell* 145, 257–267 (2011). Medline doi:10.1016/j.cell.2011.03.036

18. M. Sen, R. A. Maillard, K. Nyquist, P. Rodriguez-Aliaga, S. Pressé, A. Martin, C. Bustamante, The ClpXP protease unfolds substrates using a constant rate of pulling but different gears. *Cell* 155, 636–646 (2013). Medline

19. E. U. Weber-Ban, B. G. Reid, A. D. Miranker, A. L. Horwich, Global unfolding of a substrate protein by the Hsp100 chaperone ClpA. *Nature* 401, 90–93 (1999). Medline doi:10.1038/43481

20. A. V. Pobbati, A. Stein, D. Fasshauer, N- to C-terminal SNARE complex assembly promotes rapid membrane fusion. *Science* 313, 673–676 (2006). Medline doi:10.1126/science.1129486

21. T. Y. Yoon, B. Okumus, F. Zhang, Y. K. Shin, T. Ha, Multiple intermediates in SNARE-induced membrane fusion. *Proc. Natl. Acad. Sci. U.S.A.* 103, 19731–19736 (2006). Medline doi:10.1073/pnas.0606032103

22. R. J. Barnard, A. Morgan, R. D. Burgoyne, Stimulation of NSF ATPase activity by alpha-SNAP is required for SNARE complex disassembly and exocytosis. *J. Cell Biol.* 139, 875–883 (1997). Medline doi:10.1083/jcb.139.4.875

23. T. Ha, T. Enderle, D. F. Ogletree, D. S. Chemla, P. R. Selvin, S. Weiss, Probing the interaction between two single molecules: Fluorescence resonance energy transfer between a single donor and a single acceptor. *Proc. Natl. Acad. Sci. U.S.A.* 93, 6264–6268 (1996). Medline doi:10.1073/pnas.93.13.6264

24. Y. Park, W. Vennekate, H. Yavuz, J. Preobraschenski, J. M. Hernandez, D. Riedel, P. J. Walla, R. Jahn, α-SNAP interferes with the zippering of the SNARE protein membrane fusion machinery. *J. Biol. Chem.* 289, 16326–16335 (2014). Medline doi:10.1074/jbc.M114.556803

25. W. J. Greenleaf, M. T. Woodside, S. M. Block, High-resolution, single-molecule measurements of biomolecular motion. *Annu. Rev. Biophys. Biomol. Struct.* 36, 171–190 (2007). Medline doi:10.1146/annurev.biophys.36.101106.101451

26. J. R. Moffitt, Y. R. Chemla, S. B. Smith, C. Bustamante, Recent advances in optical tweezers. *Annu. Rev. Biochem.* 77, 205–228 (2008). Medline doi:10.1146/annurev.biochem.77.043007.090225

27. I. De Vlaminck, C. Dekker, Recent advances in magnetic tweezers. *Annu Rev Biophys* 41, 453–472 (2012). Medline doi:10.1146/annurev-biophys-122311-100544

28. T. Shimizu, K. A. Johnson, Presteady state kinetic analysis of vanadate-induced inhibition of the dynein ATPase. *J. Biol. Chem.* 258, 13833–13840 (1983). Medline

29. D. R. Davies, W. G. J. Hol, The power of vanadate in crystallographic investigations of phosphoryl transfer enzymes. *FEBS Lett.* 577, 315–321 (2004). Medline doi:10.1016/j.febslet.2004.10.022

30. Y. R. Chemla, K. Aathavan, J. Michaelis, S. Grimes, P. J. Jardine, D. L. Anderson, C. Bustamante, Mechanism of force generation of a viral DNA packaging motor. *Cell* 122, 683–692 (2005). Medline doi:10.1016/j.cell.2005.06.024

31. M. Zhao, S. Wu, Q. Zhou, S. Vivona, D. J. Cipriano, Y. Cheng, A. T. Brunger, Mechanistic insights into the recycling machine of the SNARE complex. *Nature* 518, 61–67 (2015). Medline doi:10.1038/nature14148

32. A. Stein, A. Radhakrishnan, D. Riedel, D. Fasshauer, R. Jahn, Synaptotagmin activates membrane fusion through a Ca2+-dependent trans interaction with phospholipids. *Nat. Struct. Mol. Biol.* 14, 904–911 (2007). Medline doi:10.1038/nsmb1305

33. J. M. Hernandez, A. Stein, E. Behrmann, D. Riedel, A. Cypionka, Z. Farsi, P. J. Walla, S. Raunser, R. Jahn, Membrane fusion intermediates via directional and full assembly of the SNARE complex. *Science* 336, 1581–1584 (2012). Medline doi:10.1126/science.1221976

34. M. Margittai, R. Langen, R. Jahn, SNARE-interactions in solution and in proteoliposomes studied by fluorescence spectroscopy and electron paramagnetic resonance (EPR). *Mol. Biol. Cell* 10, 209a (1999).

35. C. Cecconi, E. A. Shank, F. W. Dahlquist, S. Marqusee, C. Bustamante, Protein-DNA chimeras for single molecule mechanical folding studies with the optical tweezers. *Eur. Biophys. J.* 37, 729–738 (2008). Medline doi:10.1007/s00249-007-0247-y

36. J. C. Gebhardt, T. Bornschlögl, M. Rief, Full distance-resolved folding energy landscape of one single protein molecule. *Proc. Natl. Acad. Sci. U.S.A.* 107, 2013–2018 (2010). Medline doi:10.1073/pnas.0909854107

37. J. Kim, C. Z. Zhang, X. Zhang, T. A. Springer, A mechanically stabilized receptor-ligand flex-bond important in the vasculature. *Nature* 466, 992–995 (2010). Medline doi:10.1038/nature09295

38. H. K. Lee, Y. Yang, Z. Su, C. Hyeon, T. S. Lee, H. W. Lee, D. H. Kweon, Y. K. Shin, T. Y. Yoon, Dynamic Ca2+-dependent stimulation of vesicle fusion by membrane-anchored synaptotagmin 1. *Science* 328, 760–763 (2010). Medline doi:10.1126/science.1187722

39. J. Furst, R. B. Sutton, J. Chen, A. T. Brunger, N. Grigorieff, Electron cryomicroscopy structure of N-ethyl maleimide sensitive factor at 11 A resolution. *EMBO J.* 22, 4365–4374 (2003). Medline doi:10.1093/emboj/cdg420

40. T. M. Hohl, F. Parlati, C. Wimmer, J. E. Rothman, T. H. Söllner, H. Engelhardt, Arrangement of subunits in 20 S particles consisting of NSF, SNAPs, and SNARE complexes. *Mol. Cell* 2, 539–548 (1998). Medline doi:10.1016/S1097-2765(00)80153-7

41. W. Bae, M. G. Choi, C. Hyeon, Y. K. Shin, T. Y. Yoon, Real-time observation of multiple-protein complex formation with single-molecule FRET. *J. Am. Chem. Soc.* 135, 10254–10257 (2013). Medline doi:10.1021/ja404276g

42. K. Weninger, M. E. Bowen, S. Chu, A. T. Brunger, Single-molecule studies of SNARE complex assembly reveal parallel and antiparallel configurations. *Proc. Natl. Acad. Sci. U.S.A.* 100, 14800–14805 (2003). Medline doi:10.1073/pnas.2036428100

43. H. W. Lee, J. Y. Ryu, J. Yoo, B. Choi, K. Kim, T. Y. Yoon, Real-time single-molecule coimmunoprecipitation of weak protein-protein interactions. *Nat. Protoc.* 8, 2045–2060 (2013). Medline doi:10.1038/nprot.2013.116

44. C. E. Aitken, R. A. Marshall, J. D. Puglisi, An oxygen scavenging system for improvement of dye stability in single-molecule fluorescence experiments. *Biophys. J.* 94, 1826–1835 (2008). Medline doi:10.1529/biophysj.107.117689

45. R. Roy, S. Hohng, T. Ha, A practical guide to single-molecule FRET. *Nat. Methods* 5, 507–516 (2008). Medline doi:10.1038/nmeth.1208

46. B. Kalafut, K. Visscher, An objective, model-independent method for detection of non-uniform steps in noisy signals. *Comput. Phys. Commun.* 179, 716–723 (2008). doi:10.1016/j.cpc.2008.06.008

47. G. Tang, L. Peng, P. R. Baldwin, D. S. Mann, W. Jiang, I. Rees, S. J. Ludtke, EMAN2: An extensible image processing suite for electron microscopy. *J. Struct. Biol.* 157, 38–46 (2007). Medline doi:10.1016/j.jsb.2006.05.009

48. M. van Heel, G. Harauz, E. V. Orlova, R. Schmidt, M. Schatz, A new generation of the IMAGIC image processing system. *J. Struct. Biol.* 116, 17–24 (1996). Medline doi:10.1006/jsbi.1996.0004

49. C. Gosse, V. Croquette, Magnetic tweezers: Micromanipulation and force measurement at the molecular level. *Biophys. J.* 82, 3314–3329 (2002). Medline doi:10.1016/S0006-3495(02)75672-5

50. O. A. Saleh, J. F. Allemand, V. Croquette, D. Bensimon, Single-molecule manipulation measurements of DNA transport proteins. *ChemPhysChem* 6, 813–818 (2005). Medline doi:10.1002/cphc.200400635

51. J. Lipfert, X. Hao, N. H. Dekker, Quantitative modeling and optimization of magnetic tweezers. *Biophys. J.* 96, 5040–5049 (2009). Medline doi:10.1016/j.bpj.2009.03.055

52. K. Kim, O. A. Saleh, A high-resolution magnetic tweezer for single-molecule measurements. *Nucleic Acids Res.* 37, e136 (2009). Medline doi:10.1093/nar/gkp725

53. W. Bae, K. Kim, D. Min, J. K. Ryu, C. Hyeon, T. Y. Yoon, Programmed folding of DNA origami structures through single-molecule force control. *Nat. Commun.* 5, 5654 (2014). Medline doi:10.1038/ncomms6654

54. K. C. Neuman, A. Nagy, Single-molecule force spectroscopy: Optical tweezers, magnetic tweezers and atomic force microscopy. *Nat. Methods* 5, 491–505 (2008). Medline doi:10.1038/nmeth.1218

55. W. J. Greenleaf, M. T. Woodside, S. M. Block, High-resolution, single-molecule measurements of biomolecular motion. *Annu. Rev. Biophys. Biomol. Struct.* 36, 171–190 (2007). Medline doi:10.1146/annurev.biophys.36.101106.101451

56. A. Yildiz, J. N. Forkey, S. A. McKinney, T. Ha, Y. E. Goldman, P. R. Selvin, Myosin V walks hand-over-hand: Single fluorophore imaging with 1.5-nm localization. *Science* 300, 2061–2065 (2003). Medline doi:10.1126/science.1084398

57. J. Liphardt, S. Dumont, S. B. Smith, I. Tinoco Jr., C. Bustamante, Equilibrium information from nonequilibrium measurements in an experimental test of Jarzynski's equality. *Science* 296, 1832–1835 (2002). Medline doi:10.1126/science.1071152

58. C. Hyeon, D. Thirumalai, Can energy landscape roughness of proteins and RNA be measured by using mechanical unfolding experiments? *Proc. Natl. Acad. Sci. U.S.A.* 100, 10249–10253 (2003). Medline doi:10.1073/pnas.1833310100

59. D. Fasshauer, W. Antonin, V. Subramaniam, R. Jahn, SNARE assembly and disassembly exhibit a pronounced hysteresis. *Nat. Struct. Biol.* 9, 144–151 (2002). Medline doi:10.1038/nsb750

60. A. M. van Oijen, P. C. Blainey, D. J. Crampton, C. C. Richardson, T. Ellenberger, X. S. Xie, Single-molecule kinetics of lambda exonuclease reveal base dependence and dynamic disorder. *Science* 301, 1235–1238 (2003). Medline doi:10.1126/science.1084387

61. J. B. Lee, R. K. Hite, S. M. Hamdan, X. S. Xie, C. C. Richardson, A. M. van Oijen, DNA primase acts as a molecular brake in DNA replication. *Nature* 439, 621–624 (2006). Medline doi:10.1038/nature04317

62. S. Kim, P. C. Blainey, C. M. Schroeder, X. S. Xie, Multiplexed single-molecule assay for enzymatic activity on flow-stretched DNA. *Nat. Methods* 4, 397–399 (2007). Medline

63. C. G. Baumann, S. B. Smith, V. A. Bloomfield, C. Bustamante, Ionic effects on the elasticity of single DNA molecules. *Proc. Natl. Acad. Sci. U.S.A.* 94, 6185–6190 (1997). Medline doi:10.1073/pnas.94.12.6185

64. N. Forns, S. de Lorenzo, M. Manosas, K. Hayashi, J. M. Huguet, F. Ritort, Improving signal/noise resolution in single-molecule experiments using molecular constructs with short handles. *Biophys. J.* 100, 1765–1774 (2011). Medline doi:10.1016/j.bpj.2011.01.071

65. T. Bornschlögl, M. Rief, Single molecule unzipping of coiled coils: Sequence resolved stability profiles. *Phys. Rev. Lett.* 96, 118102 (2006). Medline doi:10.1103/PhysRevLett.96.118102

66. A. Stein, G. Weber, M. C. Wahl, R. Jahn, Helical extension of the neuronal SNARE complex into the membrane. *Nature* 460, 525–528 (2009). Medline

67. M. T. Woodside, W. M. Behnke-Parks, K. Larizadeh, K. Travers, D. Herschlag, S. M. Block, Nanomechanical measurements of the sequence-dependent folding landscapes of single nucleic acid hairpins. *Proc. Natl. Acad. Sci. U.S.A.* 103, 6190–6195 (2006). Medline doi:10.1073/pnas.0511048103

68. C. Joo, S. A. McKinney, M. Nakamura, I. Rasnik, S. Myong, T. Ha, Real-time observation of RecA filament dynamics with single monomer resolution. *Cell* 126, 515–527 (2006). Medline doi:10.1016/j.cell.2006.06.042

69. G. Oster, Brownian ratchets: Darwin's motors. *Nature* 417, 25 (2002). Medline doi:10.1038/417025a